

# SIMULATING ACCRETION PROCESSES IN STAR-FORMATION



FOLLOWING ACCRETION PROCESSES IN  
SIMULATIONS OF STAR-FORMATION USING SINK  
PARTICLES

By

VICTOR KUMAR ARORA, B.Sc.

A Thesis

Submitted to the School of Graduate Studies

in Partial Fulfilment of the Requirements

for the Degree

Master of Science

McMaster University

©Copyright by Victor Arora, 2009

MASTER OF SCIENCE (2009)  
(Department of Physics and Astronomy)

McMaster University  
Hamilton, Ontario

TITLE: FOLLOWING ACCRETION PROCESSES IN SIMULATIONS  
OF STAR-FORMATION USING SINK PARTICLES

AUTHOR: Victor Arora, B.Sc.

SUPERVISOR: Dr. James W. Wadsley

NUMBER OF PAGES: xi, 71

# Abstract

Resolving the wide range of spatial scales simultaneously present in the formation of stars and star clusters is a challenge for numerical simulations. Methods such as adaptive hydrodynamics codes must be used in many gas-dynamical simulations where gravity is also present, and constructs known as “sinks” are commonly used to avoid the computational expense of directly simulating the dense regions within protostars. Despite being essential to investigations of star formation over long timescales, numerics can often play an undesired role in the behaviour of these point-mass accretors, causing artificial accretion. In this thesis, the use of sink particles as models of protostars is investigated using the Gasoline  $N$ -body + smoothed particle hydrodynamics code. Motivated by observations of disks and accretion rates onto protostars, physical viscosity using the  $\alpha$ -parametrization was implemented. Tests of both spherical and rotating protostellar accretion were performed. In spite of their importance to star formation, previously presented rotating tests are subject to several numerical problems; efforts were made in this work to simulate a three-dimensional viscous accretion disk where such issues were identified and minimized. Simulations were performed for varying strengths of viscosity and sink radius, as well as with inner boundary conditions known as “sinking” particles. Angular momentum transport was present and behaved physically in all cases with  $\alpha > 0$ , and the average radial velocities and mass-accretion rates in the disks matched finite-difference estimates of corresponding analytic expressions.

# Acknowledgements

To my supervisor, James Wadsley, thank you for allowing me this opportunity, and guiding me through this interesting and challenging topic. The discussions we had were greatly helpful to me, and your suggestions during the construction of this thesis were essential to its completion.

I'd also like to thank my thesis committee members, Alison Sills and Laura Parker for taking the time to review and comment on this work.

Finally, I would like to thank all of my past and present office-mates and friends in the department for their contributions.

This work was made possible by the facilities of the Shared Hierarchical Academic Research Computing Network (SHARCNET:[www.sharcnet.ca](http://www.sharcnet.ca)) and has made use of NASA's Astrophysics Data System Bibliographic Services.

*Dedicated to my parents Usha and Vijay.  
I could not have completed this work without your love and support.  
Thank you for everything.*

# Table of Contents

<b>Abstract</b>	iii
<b>Acknowledgements</b>	iv
<b>List of Figures</b>	viii
<b>List of Tables</b>	xi
<b>Chapter 1 Introduction</b>	<b>1</b>
1.1 Star Formation: the Origin of the IMF . . . . .	1
1.2 Accretion Disks . . . . .	3
1.2.1 Accretion Disks: Viscous Transport . . . . .	4
1.2.2 The $\alpha$ -prescription . . . . .	7
1.2.3 Theory of Ideal Disks . . . . .	9
1.3 Sink Particles . . . . .	10
1.3.1 Bate, Bonnell, & Price (1995) . . . . .	11
1.3.2 Krumholz, McKee, & Klein (2004) . . . . .	13
1.3.3 Bromm, Coppi, & Larson (2002) . . . . .	15
1.4 Overview . . . . .	15
<b>Chapter 2 Methods</b>	<b>17</b>
2.1 Smoothed Particle Hydrodynamics . . . . .	17
2.1.1 Gas Dynamics . . . . .	17

2.1.2	The SPH Method . . . . .	21
2.1.3	Viscosity in SPH . . . . .	25
2.1.4	Sinking Particles . . . . .	27
2.2	Constructing Initial Conditions . . . . .	29
2.2.1	Singular Isothermal Sphere . . . . .	31
2.2.2	Keplerian Ring . . . . .	31
2.2.3	Accretion Disk . . . . .	32
<b>Chapter 3 Results</b>		<b>36</b>
3.1	Isothermal Collapse . . . . .	36
3.2	Viscous Keplerian Ring . . . . .	40
3.3	Viscous Accretion Disks . . . . .	43
3.3.1	Fiducial Case: $\alpha = 0.1, r_{\text{acc}} = 0.05$ . . . . .	43
3.3.2	No-sink Case . . . . .	53
3.3.3	Varying $\alpha$ . . . . .	55
3.3.4	Varying the Accretion Radius . . . . .	57
3.3.5	Sinking Particles as a Boundary Condition . . . . .	60
3.3.6	Angular Momentum Distribution . . . . .	64
<b>Chapter 4 Conclusion</b>		<b>66</b>
4.1	Future Work . . . . .	69

# List of Figures

2.1	“Sinking particles” inner boundary condition . . . . .	30
2.2	The initial state for accretion disk simulations . . . . .	34
3.1	Density and radial velocity profiles of the SIS at different fractions of $t_{collapse}$ . . . . .	38
3.2	The accretion of mass by the central sink particle in the SIS as a function of time . . . . .	39
3.3	The surface density of a viscous Keplerian ring at various dimen- sionless times . . . . .	42
3.4	The surface density of an inviscid Keplerian ring at various orbital times . . . . .	43
3.5	The azimuthally averaged surface density of an $\alpha = 0.1$ accretion disk at various times . . . . .	46
3.6	Best fits to the surface density profile of an $\alpha = 0.1$ accretion disk at $t = 1.4T$ . . . . .	47
3.7	A comparison of the total $z$ -component of the angular momentum in the fiducial disk at various times . . . . .	48
3.8	The particle distribution of radial velocities in the fiducial disk at $t = 10T$ . . . . .	49
3.9	The mean radial velocity measured in radial bins in the fiducial disk at $t = 10T$ . . . . .	50

3.10	The accretion rate in the fiducial disk as a function of position . . .	51
3.11	The sink mass and its accretion rate as a function of time in the fiducial case. . . . .	53
3.12	The components of the tangential acceleration in the fiducial disk at the end of the run . . . . .	54
3.13	The mass contained within $r < 0.05$ and the accretion rate for that region as a function of time in the no-sink case . . . . .	55
3.14	The mean radial velocities and mass accretion rates at $t = 10T$ measured in the disks evolved with $\alpha = 0.2$ and $0.4$ . . . . .	56
3.15	A comparison of the sink mass as a function of time for the disks evolved with $\alpha = 0, 0.1, 0.2,$ and $0.4.$ . . . . .	58
3.16	A comparison of the mass contained within $r = 0.1$ and the accre- tion rate for that region as a function of time for the fiducial case and the $r_{\text{acc}} = 0.1$ case . . . . .	59
3.17	A comparison of the mass accretion rates in the disk for the fiducial case and the $r_{\text{acc}} = 0.1$ case . . . . .	60
3.18	A comparison of the radial velocity in the fiducial case and the case with a sinking-particles boundary condition . . . . .	61
3.19	A comparison of the mass accretion rate in the fiducial disk and the case with a sinking-particles boundary condition . . . . .	62
3.20	A comparison of the sink mass as a function of time in the fiducial, no-sink, and sinking-particles boundary condition case. . . . .	63

3.21 A comparison of the total  $z$ -component of the final angular momentum in the fiducial disk, the sinking-particles disk, and the standard sink disk . . . . . 64

# List of Tables

3.1	Comparing the final sink mass for the various models tested . . .	65
-----	---	----



# Chapter 1

## Introduction

### 1.1 Star Formation: the Origin of the IMF

Important quantitative measures of star-formation such as the initial mass function (IMF), multiplicity, and the formation times of different stellar populations in a cluster are likely determined by how self-gravitating regions form in molecular clouds, and how the matter accretes within these regions. While analytical methods are always best, they are often only appropriate to use in idealized situations. One must turn to numerical simulations to attempt to solve the highly coupled non-linear physics of star-formation. For example, the molecular clouds out of which stars are eventually born are generally thought to be turbulent (Larson, 1981), but turbulence is a physical process for which an analytic theory does not exist.

There are currently two main origin models for the IMF in star clusters competing in the literature (see Klessen et al. (2009) and Bonnell et al. (2007) for recent reviews) that use different fluid dynamics formulations. Smoothed particle hydrodynamics codes (SPH: see §2.1.2) follow individual elements of

the fluid, whereas grid codes discretize the simulation volume into fixed cells through which fluxes of fluid quantities are calculated. In the competitive accretion model (e.g., Bate et al., 2003; Bate & Bonnell, 2005), SPH simulations show that the characteristic mass of the IMF is set by a combination of the thermal Jeans mass  $M_J$  for gravitational fragmentation (as defined in Binney & Tremaine (1987)):

$$M_J = \frac{\pi^{5/2}}{6} c_s^3 G^{-3/2} \rho^{-1/2} \quad (1.1)$$

(where  $c_s = (\gamma P/\rho)^{1/2}$  is the local sound speed of the gas,  $P$  is the thermal gas pressure,  $\rho$  is the mass-density, and  $\gamma$  is the ratio of specific heats, or the adiabatic index), and the density at which dust opacity in the self-gravitating gas becomes significant (the “opacity limit<sup>1</sup>”). All protostellar systems begin at this same mass and accrete gas from their natal surroundings (a “bottom-up” paradigm). High-mass stars form in the centre of star clusters, since the gravitational potential there attracts the most gas. Protostars that are ejected from the central regions by close encounters with other protostars are unable to accrete as much gas, thus forming the low-mass population.

The turbulent fragmentation model (e.g., Padoan & Nordlund, 2002), developed mainly using grid simulations, proposes that the IMF is specified by the statistical properties of turbulence. The probability distribution function for supersonic turbulence can create a power-law spectrum of density

---

<sup>1</sup> The opacity limit is a minimum value for this characteristic mass. A collapsing protostellar core that reaches this stage can no longer efficiently radiate away the gravitational potential energy that is liberated as it contracts. This alters the equation-of-state of the gas from isothermal to adiabatic, making the core stable to further fragmentation (Low & Lynden-Bell, 1976; Masunaga & Inutsuka, 1999; Bate et al., 2003).

enhancements. Some of these regions will be dense enough to become self-gravitating (Mac Low & Klessen, 2004) and collapse to form protostars (a “top-down” paradigm). This is often framed as arguing that turbulence sets the bound prestellar-core mass function, which can be directly mapped to the IMF subject to an efficiency factor. Matzner & McKee (2000) and Shu et al. (2004) calculate efficiency factors of  $\sim 30\%$  due to feedback from protostellar outflows; observations of molecular cores in the Pipe Nebula suggest a similar efficiency (Alves et al., 2007).

Both theories are able to reproduce the qualitative picture of the IMF. An interesting point is that both competitive accretion and turbulent fragmentation seem to play to the specialities of the numerical method out of which the theory was born (respectively, incorporating sink particles in SPH, and simulating turbulence in grid codes). The addition of more physics (such as different types of feedback, chemistry models, etc.) along with improved resolution will hopefully help to break the degeneracies between these models.

## 1.2 Accretion Disks

Self-gravitating cores of dense, cool molecular gas are thought to be the precursor to main-sequence stars. The observed physical parameters of cores vary within and amongst star-forming regions, with temperatures  $T \sim 8 - 12$  K, masses  $m \sim 0.2 - 20 M_{\odot}$ , and radii  $r \sim 0.02 - 0.2$  pc (Bergin & Tafalla, 2007; Ward-Thompson et al., 2007; Lada et al., 2008). As these cores collapse gravitationally down to objects several million times smaller, even very slow rotation in the progenitor cores will be greatly amplified, exceeding the rate a

star can withstand without breaking apart. Angular momentum conservation dictates that a disk will form; only parts of the core with high specific angular momentum will be able to counteract the inward gravitational acceleration, and only in directions perpendicular to the axis of rotation. Dissipation will settle opposing vertical gas motions into a flat disk (de Pater & Lissauer, 2001; Clarke & Carswell, 2007). Observations suggest that young protoplanetary disks (i.e. surrounding T Tauri, or pre-main-sequence stars) have masses in the range  $0.001 - 0.1 M_{\odot}$  (Andrews & Williams, 2005) and outer radii of  $\sim 200$  AU from submillimeter dust-continuum measurements (Andrews & Williams, 2007), although molecular gas observations indicate material with high specific angular momentum at  $\lesssim 800$  AU (Mundy et al. 2000; also see §1.2.1). Statistical studies have suggested lifetimes for these disks of  $\lesssim 6$  million years (Haisch et al., 2001). Dusty debris disks have also been directly imaged around young ( $\sim 10 - 100$  Myr) main-sequence stars at optical wavelengths (e.g., Smith & Terrile, 1984; Kalas et al., 2004, 2005). Disk masses derived from submillimetre imaging show that these disks only have up to a few lunar masses of dusty material, suggesting any possible planet formation will have already taken place in these systems (Holland et al., 1998; Kalas et al., 2004).

### 1.2.1 Accretion Disks: Viscous Transport

Gas in an accretion disk is in centrifugal balance. This directly leads to the conclusion that the angular velocity  $\Omega$  in the disk is Keplerian, or proportional to  $r^{-3/2}$ . As the gas rotates in such a differentially rotating disk,

random motions cause gas parcels to diffuse across streamlines, redistributing momentum; this mechanism is known as shear viscosity.

Dissipative interactions within a disk will cause some of the orbital energy in the gas to be thermalized (converted to internal, or thermal energy). Further, the radiative cooling timescale for the gas is often assumed to be fast (compared to the timescale for the transport of angular momentum), so the gas will readily lose orbital energy until the orbit is circularized. In order to be accreted by the central star, gas in the disk must then move to a lower orbit by losing angular momentum. As parcels of gas in the disk slide past one another, a radially exterior streamline will experience a viscous torque due to a radially interior streamline, gaining angular momentum at its expense. Gas in the interior streamline can sink lower in the potential well, and as it continues to lose orbital energy and angular momentum, it will spiral inward in the disk where it is eventually accreted by a protostar. Gas in the exterior streamline can in turn transfer angular momentum to a streamline further exterior and so on, causing angular momentum to be transported outward in the disk (Frank et al., 1985).

The question of what form of viscosity may be present in accretion disks is an open one. “Molecular” viscosity, defined as viscous interactions associated with a length scale of order the mean free path of molecules  $\ell$  moving with random thermal velocities  $\sim c_s$  (Frank et al., 1985; Clarke & Carswell, 2007), is almost always present in real fluids. The dimensionless Reynolds number  $Re$  can be defined as a ratio of inertial to non-inertial, or viscous, terms in the Navier-Stokes momentum equation (2.6) (Frank et al., 1985), or by simply

constructing a ratio using a characteristic length scale  $L$  and velocity scale  $V$  for the flow at a given viscosity  $\nu$  (Landau & Lifshitz, 1987):

$$Re = \frac{LV}{\nu} = \frac{LV}{c_s \ell} = \frac{LV}{c_s (n\sigma_m)^{-1}} \quad (1.2)$$

where we have approximated the molecular viscosity  $\nu \sim c_s \ell$  as interacting over a distance given by the product of the number density  $n$  of molecules and the cross-section  $\sigma_m$  for their interaction. Adopting values derived from a minimum mass solar nebula (MMSN) disk model (Hayashi, 1981) for gas at  $L = 1$  AU, the circular velocity  $V \approx 3 \times 10^6$  cm s<sup>-1</sup> at 1 AU, a sound speed of  $c_s \approx 10^5$  cm s<sup>-1</sup>, a number density of  $n \approx 4 \times 10^{14}$  cm<sup>-3</sup>, and the collisional cross section for molecular hydrogen  $\sigma_m = 2 \times 10^{-15}$  cm<sup>2</sup> (Chapman & Cowling, 1970) gives a Reynolds number of  $Re \sim 10^{14}$ . Since  $Re \gg 1$ , this suggests that molecular viscosity is negligible in accretion disks; in fact, accretion due to molecular viscosity alone gives timescales for angular momentum transport in a MMSN disk that are greater than a Hubble time (Clarke & Carswell, 2007). The magnitude of the Reynolds number is also indicator of turbulence in a flow; laboratory fluids typically become turbulent beyond  $Re \sim 10 - 10^3$ , suggesting that accretion disks are most likely turbulent (Frank et al., 1985; Clarke & Carswell, 2007).

The magnetorotational instability (MRI) has been proposed as a source of the turbulence in magnetized disks (Balbus & Hawley, 1991). It can be shown (Balbus, 2003) that magnetized disks are stable to growth of perturbations in the orbital plane if and only if the criterion:

$$\frac{d\Omega^2}{dR} \geq 0 \quad (1.3)$$

where  $\Omega$  is the angular velocity and  $R$  the radial distance from the rotation axis, is satisfied at all points in the disk. The criterion (1.3) is not satisfied for Keplerian disks since  $\Omega \propto r^{-3/2}$ , implying that this instability may be common among astrophysical disks. Magnetic field lines connecting neighbouring fluid elements act analogously to a simple spring. If the elements are radially displaced, the torques exerted by this spring-like force act as a mediator for viscous transport; further, as the radial displacement increases, the tension increases alike, thus increasing the torques, which (for a sufficiently weak spring/magnetic field) leads to a runaway process. The non-linear growth of the instability results in the onset of sustained turbulence (Hawley et al., 1995). The random bulk motions caused by turbulence act as an effective viscosity associated with scales equal to the size of the largest turbulent eddies, as well as the turnover velocity (Frank et al., 1985), although unlike purely hydrodynamic turbulence, energy can be transported to both smaller and larger scales for turbulence arising from the MRI.

In disks where self-gravity is significant, gravitational torques due to spiral modes or gravitational instability in the disk can also be an effective transport mechanism over large spatial scales (e.g, Lodato & Rice, 2004), although such instabilities may be short-lived ( $\sim 10^6$  years) depending on the strength of any viscosity present (Vorobyov & Basu, 2009).

### 1.2.2 The $\alpha$ -prescription

The kinematic viscosity,  $\nu$ , is equal to the dynamic, or shear viscosity coefficient  $\eta$  divided by the fluid density  $\rho$ , and is non-zero in the presence of

a shearing flow (see also the discussion following equation (2.5)). In general, the kinematic viscosity may vary with radius in the disk, however, as noted in §1.2.1, the source of the viscosity in accretion disks is not well-constrained, leaving the functional form unknown. Shakura & Sunyaev (1973) introduced a parametrization for the kinematic viscosity based on dimensional arguments. Assuming that the effective viscosity in accretion disks is turbulent in nature, one can reason that the largest turbulent eddies can be no larger than the disk scale-height  $H = c_s/\Omega$  where  $c_s$  is the sound speed and  $\Omega$  is the angular velocity (see also equation (2.29)). One can further argue that the maximum speed at which the flow can become turbulent is the sound speed  $c_s$  (Frank et al., 1985). The product of these quantities has dimensions appropriate to viscosity, and the dimensionless  $\alpha$  parameter is introduced to scale the proportionality, giving:

$$\nu = \alpha c_s H \tag{1.4}$$

Using this allows one to approximate the effect of a viscosity of varying magnitudes in a calculation without detailed knowledge of the source.

Typical values for  $\alpha$  can vary but are less than unity in stable disks by construction. Hartmann et al. (1998) find  $\alpha \sim 0.01$  for disks around T Tauri stars over scales of 10 – 100 AU. There is also the possibility of  $\alpha$  varying throughout the disk; using a similar technique as the Hartmann et al. group, Isella et al. (2009) found that  $\alpha$  decreases with radius from as large as  $\alpha = 0.5$  at 1 AU to as small as  $\alpha = 10^{-4}$  at 100 AU in disks around pre-main-sequence stars. Theoretical models (MRI) predict values over a similar range of  $\alpha = 5 \times 10^{-3} - 0.6$  (Balbus, 2003). Groups studying gravitational instability as a

transport mechanism have determined effective values of  $\alpha = 0.05$  (Lodato & Rice, 2004). Vorobyov & Basu (2009) have found from two-dimensional models of viscous self-gravitating disks, that the dominant mode of transport depends on the size of the viscous  $\alpha$ . They find an effective  $\alpha$  due to gravitational torques of  $\sim 10^{-4} - 10^{-3}$  for nearly inviscid self-gravitating disks. Viscous transport becomes dominant in their disks for  $\alpha > 10^{-2}$ .

### 1.2.3 Theory of Ideal Disks

The equations governing the radial structure of a thin axisymmetric accretion disk are given below, following Frank, King, & Raine (1985, Ch. 5). Define  $R$  as the usual radial displacement in cylindrical coordinates,  $v_R$  the velocity in the radial direction, and  $\Sigma = \int_{-\infty}^{\infty} \rho dz$  as the surface density of the disk, where  $\rho$  is the volume mass-density. Imposing mass conservation,

$$R \frac{\partial \Sigma}{\partial t} + \frac{\partial}{\partial R} (R \Sigma v_R) = 0 \quad (1.5)$$

the equation for conservation of angular momentum in the disk, including transport due to the net effect of viscous torques  $G$ ,

$$R \Sigma v_r \frac{\partial}{\partial R} (R^2 \Omega) = \frac{1}{2\pi} \frac{\partial G}{\partial R} \quad (1.6)$$

where

$$G(R, t) = 2\pi R \nu \Sigma R^2 \frac{\partial \Omega}{\partial R} \quad (1.7)$$

and assuming Keplerian angular velocities  $\Omega = \sqrt{GM/R^3}$  (where  $G$  here is Newton's gravitational constant), the evolution of the surface density of the disk is determined by:

$$\frac{\partial \Sigma}{\partial t} = \frac{3}{R} \frac{\partial}{\partial R} \left\{ R^{1/2} \frac{\partial}{\partial R} [\nu \Sigma R^{1/2}] \right\} \quad (1.8)$$

Using (1.6) and (1.7) one can find an expression for the radial velocity:

$$v_R = -\frac{3}{\Sigma R^{1/2}} \frac{\partial}{\partial R} [\nu \Sigma R^{1/2}] \quad (1.9)$$

which is, as expected, dependent on the viscosity in the disk. The radial mass-flux (or accretion rate) at a point  $R$  in the disk is then related to the viscosity through the radial drift velocity by:

$$\dot{M}(R) = -2\pi R \Sigma v_R \quad (1.10)$$

### 1.3 Sink Particles

At some point in the star formation process, gravity will cause gas to accrete onto a much denser protostar. During this time, commonly observed statistical measures such as the initial mass function and stellar multiplicity are likely determined to some degree, perhaps by dynamical interactions with the larger star-forming environment. In such accretion processes, mass-density increases, posing a problem for numerical studies. The Courant stability condition:

$$\Delta t = \frac{\Delta x}{\Delta c_s} \sim \frac{h}{c_s} \quad (1.11)$$

is one of the criteria<sup>2</sup> used to define the largest locally allowable timestep in a hydrodynamical simulation, where  $\Delta x$  is the width of a resolution element (equivalent to the “smoothing length” scale  $h$  in Smoothed Particle Hydrodynamics further discussed in §2.1.2), and  $c_s$  is the local sound speed (or more

---

<sup>2</sup> Additional timestep criteria are invoked in this work that take into account the acceleration, viscous forces, and expansion cooling of the fluid element being modelled (see Wadsley et al. (2004) for details).

generally, the maximum local wave speed). The condition (1.11) can be understood as requiring that the domain of numerical dependence include the domain of physical dependence. In other words, this imposes a limit on the extent to which a signal may propagate during a timestep.

It is clear that, as density  $\rho$  increases,  $\Delta t$  must decrease (note that  $\Delta x$  also decreases with increasing  $\rho$  for adaptive methods). In star-formation however, the range in densities required between the initial state ( $\rho_{\text{GMC}} \sim 10^{-21} \text{ g cm}^{-3}$ ) and end-point ( $\rho_{\odot} \sim 1 \text{ g cm}^{-3}$ ) means that as protostars form, timesteps in the densest regions must be reduced to increasingly smaller intervals, effectively halting the entire simulation. In fact this is true for almost any dynamical time used to set the timesteps (e.g. the orbital time of particles in a Keplerian disk gives  $\Delta t \sim r^{3/2}$ ).

The simplest workaround to this problem is to manually limit the resolution of a simulation. As the number of particles at this minimum density increase however, the order of the calculation can increase locally, which can also halt a simulation. If modelling such dense objects is not of primary interest, “sink” particles are frequently invoked to replace these regions and prevent densities from increasing, allowing the simulation to continue. Sink particles only interact with gas in a simulation gravitationally. A variety of methods have been suggested to implement sink particles.

### 1.3.1 Bate, Bonnell, & Price (1995)

A collisionless point-mass sink particle is introduced to replace dense, collapsing regions of gas. An accretion radius  $r_{\text{acc}}$  for the sink is defined at run

time that effectively sets the hydrodynamic resolution near the sink. Accretion onto the sink is based on the following criteria for gas particles passing within the accretion radius:

1. The gas particle must be bound to the sink (i.e. potential energy + kinetic energy  $< 0$ ), and more tightly than to any other sink in the simulation volume.
2. The specific angular momentum of the gas particle with respect to the centre of the sink must be less than that required to form a circular orbit at  $r_{\text{acc}}$  – in other words, it must be on a decaying/plunging orbit.

Mass, as well as linear and angular momenta from accreted particles, are transferred to the sink, and the gas particles are removed from the simulation. These sinks also consume the thermal energy from accreted particles that would otherwise go into heating the gas.

An evacuated region is created around a sink due to the absence of particles within the accretion radius. Particles near the edge of the sink therefore see fewer neighbouring particles, leading to errors in the determination of density and pressure. Also, angular momentum transport in disks depends on there being material to transport it from/to; the unresolved region in a sink can therefore corrupt this process, causing unphysical accretion. Since mass is a primary observable in star-formation (see §1.1), it is essential that accretion onto a sink is physical.

Boundary conditions have been described that are designed to correct for these errors. For a given gas particle, the general method is to estimate the

gradient for a quantity from its neighbours and correct for the missing contribution to that quantity (Bate et al., 1995). In the case of pressure and viscous acceleration corrections, an equal and opposite force is applied to the sink; however, due to concerns about the treatment of viscous accretion and potentially unlimited angular momentum transfer out of the sink, these boundary conditions are in fact no longer used by the author (priv. comm.).

Tests were presented examining the accretion rate onto central sinks in disks. Results with boundary conditions reduced the amount of artificial accretion, but did not quite bring the final sink masses in line with a non-sink result for the total mass “accreted”, suggesting that they could be improved. The results seemed to indicate that angular momentum transport is dependent on the choice of accretion radius, thus changing the final sink masses. The only viscous interaction present in these tests was the explicit artificial viscosity used in SPH (see §2.1.3.1). This however is problematic due to its non-linearity, and resolution dependence (equation (2.19)). The accretion rate and results of the simulation, are by extension also dependent on resolution.

These sinks have been included in a number of star cluster formation simulations investigating the stellar IMF (Bate et al., 2003; Bate, 2009a,b), and brown dwarfs (Bate et al., 2002; Bonnell et al., 2008).

### 1.3.2 Krumholz, McKee, & Klein (2004)

A sink is again represented by a point-mass non-gaseous accreting particle. An analytically determined accretion rate is used to set the amount of mass to be removed from an accretion “zone”, (and effectively the back-pressure oppos-

ing the accretion). Sink accretion is modelled as Bondi-Hoyle accretion (Hoyle & Lyttleton, 1939; Bondi & Hoyle, 1944; Bondi, 1952), defined as spherical accretion onto an object moving with respect to a background flow, implemented using the approximate accretion rate given in Ruffert (1994). For anisotropic accretion and rotating flows, radial velocity and angular momentum are both preserved in the gas, in contrast to the Bate et al. method. Some angular momentum, however, must be lost from the gas in an accretion disk in order to explain the outflows observed in many young stellar objects.

Tests presented for spherical accretion (based on the singular isothermal sphere of Shu (1977)) were well-handled, with deviations of a few percent from the analytic expectations for density, velocity and accretion rate. A rotating ring test performed however revealed the presence of a significant resolution dependent viscosity, in other words, numerical diffusion. Since this numerical viscosity is implicit, it can be difficult to characterize. A disk test performed likely suffers from unphysical transport due to this diffusion, as well as other numerical problems, such as an unresolved scale-height at the edge of the accretion zone. As well, the disk was only simulated for about 0.4 periods at the edge of the disk, which is not long enough to fully examine global disk dynamics.

In addition to the tests discussed in Krumholz et al. (2004), this methodology for sinks has been extended to include a more detailed protostellar model (specifying characteristics such as stellar radius and luminosity) for use in a radiation hydrodynamics code (Krumholz et al., 2007b). This has been ap-

plied to studies of the collapse and fragmentation of massive cores as well as individual massive-stellar systems (Krumholz et al., 2007a, 2009)

### 1.3.3 Bromm, Coppi, & Larson (2002)

Particles in dense regions are merged to form a single massive gaseous particle. Bromm et al. claim that the particle is over-pressured compared to its surroundings, preventing spurious accretion. In the limit of a very large mass, the particle behaves as if it were collisionless. This methodology was presented in the context of examining the collapse and fragmentation of a primordial, metal-free molecular cloud.

## 1.4 Overview

Accretion rates observed in protostars suggest that disks are dominated by viscosity, however this is not modelled in many simulations. In chapter 2, a review of viscous hydrodynamics and the SPH numerical method used in this work, including an implementation of physical viscosity, is presented. An overview of the methodology used to construct initial conditions for the simulations performed is also presented. As well, the various models for sinks used in these simulations are described. In chapter 3, results from these simulations are presented along with accompanying discussion. The spreading of a viscous ring in orbit is presented as a test of the physical viscosity implementation in SPH. Simulations are also performed for the collapse of an isothermal sphere, and the structural evolution of a three-dimensional accretion disk. These cor-

respond to the two major modes of quiescent accretion in protostars: spherical collapse and azimuthal accretion. Although there are likely times during the formation of stars in which the accretion fluctuates (e.g., Vorobyov & Basu, 2009), simulating these “simpler” cases allows for comparison with known solutions, and the identification of any numerical issues. In chapter 4, the results from these simulations along with possible implications are summarized, along with some speculative remarks on future work.

## Chapter 2

### Methods

#### 2.1 Smoothed Particle Hydrodynamics

##### 2.1.1 Gas Dynamics

Gas flows of Mach number  $\mathcal{M} \gtrsim 1$  (where  $\mathcal{M} = v/c_s$  is the gas bulk speed  $v$  in units of the local sound speed  $c_s$ ) are frequently present in astrophysical fluids. As such, interstellar gases must be modelled using the machinery of compressible fluid dynamics. A system of conservation laws describing these gases can be developed for mass, momentum, and energy, known as the Euler equations (e.g. Landau & Lifshitz, 1987; Chorin & Marsden, 1990; Clarke & Carswell, 2007). The system can be closed by choosing an appropriate equation of state.

Conservation of mass is expressed through the continuity equation:

$$\frac{\partial \rho}{\partial t} + \nabla \cdot (\rho \vec{v}) = 0$$

or

$$\frac{d\rho}{dt} + \rho \nabla \cdot \vec{v} = 0 \quad (2.1)$$

where  $\rho$  is the local fluid mass-density, and  $\vec{v}$  is the flow velocity. The full time- or material-derivative in hydrodynamics is defined as:

$$\frac{d}{dt} = \frac{\partial}{\partial t} + \vec{v} \cdot \nabla \quad (2.2)$$

The extra term in the full time-derivative is due to the advection of the parcel of fluid under consideration.

The momentum evolution equation describes the rate of change of momentum for an inviscid fluid:

$$\frac{d\vec{v}}{dt} = -\frac{\nabla P}{\rho} + \vec{g} \quad (2.3)$$

where  $P$  denotes the thermal gas pressure and  $\vec{g}$  represents external “body-forces” per unit mass (i.e. accelerations) such as gravity.

More generally, the pressure force can be included with other surface forces in the momentum equation as part of the stress tensor  $\tau_{\alpha\beta}$  written using the standard summation convention:

$$\tau_{\alpha\beta} = (-P\delta_{\alpha\beta} + \sigma_{\alpha\beta}) \quad (2.4)$$

where the  $\alpha$  and  $\beta$  subscripts represent spatial coordinates (e.g.  $\alpha \in \{x, y, z\}$  in Cartesian coordinates) and  $\delta_{\alpha\beta}$  is the Kronecker delta. The stress tensor is symmetric, with the pressure supplying the diagonal components. The stress tensor can also include components, by virtue of the term  $\sigma_{\alpha\beta}$ , that describe the transfer of momentum between fluid parcels due to viscous diffusion; this term is known as the viscous-stress tensor:

$$\sigma_{\alpha\beta} = \eta \left( \frac{\partial v_\alpha}{\partial x_\beta} + \frac{\partial v_\beta}{\partial x_\alpha} - \frac{2}{3} \delta_{\alpha\beta} \nabla \cdot \vec{v} \right) + \zeta \delta_{\alpha\beta} \nabla \cdot \vec{v} \quad (2.5)$$

where  $\eta$  and  $\zeta$  are the dynamic and bulk viscosity coefficients respectively. Single subscripts denote vector components, and the generalized spatial coordinate  $x$  is used in equation (2.5), hence a derivative with respect to  $x_\alpha$  is understood to mean “with respect to any spatial coordinate labelled by  $\alpha$ ”. The first part of the tensor (2.5) describes the dynamic viscosity (commonly known as the shear viscosity) which is present in regions of velocity gradients perpendicular to the direction of flow (e.g. in accretion disks); the second part of this tensor describes the bulk viscosity which operates in the direction of flow, and is important in compressive regions of the gas (such as shock fronts). Including this in equation (2.3), we re-define the momentum equation as:

$$\frac{d\vec{v}}{dt} = -\frac{\nabla P}{\rho} + \vec{g} + \frac{\nabla\vec{\sigma}}{\rho} \quad (2.6)$$

where  $\nabla\vec{\sigma}$  is  $\partial\sigma_{\alpha\beta}/\partial x_\beta$ .

For non-isothermal viscous or supersonic flows, an energy equation is also necessary. The rate of change of total energy  $\rho E$  within a given volume is the sum of three things: external heating (or cooling)  $q$  per unit volume, the work done by body-forces (on the volume) and by forces at the bounding surface for that volume (such as pressure and viscosity), and the energy flux through the surface. The result (using the summation convention) is:

$$\frac{\partial}{\partial t}(\rho E) = \rho q + \rho v_\alpha g_\alpha + \frac{\partial}{\partial x_\beta}(v_\alpha \tau_{\alpha\beta}) - \frac{\partial}{\partial x_\alpha}(\rho v_\alpha E) \quad (2.7)$$

While total energy  $\rho E$  is the conserved quantity, equation (2.7) can be further decomposed into relations for the specific kinetic energy  $\frac{1}{2}\|v^2\|$ :

$$\rho \frac{d(\frac{1}{2}\|v^2\|)}{dt} = \frac{\partial}{\partial x_\beta}(v_\alpha \tau_{\alpha\beta}) + \rho \vec{v} \cdot \vec{g} \quad (2.8)$$

and specific internal (thermal) energy  $u$ , using the first law of thermodynamics:

$$du = Tds - PdV \quad (2.9)$$

where  $T$  is the gas temperature,  $ds$  is the infinitesimal entropy change per unit mass, and  $dV$  is the infinitesimal specific volume (i.e. per unit mass). Converting all terms to time-derivatives, and using  $dV = d(\rho^{-1})$  allows replacing the adiabatic work term  $PdV$  with  $-P/\rho^2 d\rho$ :

$$\frac{du}{dt} = T \frac{ds}{dt} + \frac{P}{\rho^2} \frac{d\rho}{dt} \quad (2.10)$$

and applying the continuity equation (2.1) gives:

$$\frac{du}{dt} = T \frac{ds}{dt} - \frac{P}{\rho} \nabla \cdot \vec{v} \quad (2.11)$$

The irreversible processes contributing to the  $Tds$  term are specified as the viscous dissipation of heat, conduction, and external processes. Combining these processes with the  $PdV$  work in equation (2.11) gives:

$$\frac{du}{dt} = -\frac{P}{\rho} \nabla \cdot \vec{v} + \psi + \frac{1}{\rho} \nabla \cdot (\kappa \nabla T) + q \quad (2.12)$$

where  $\kappa$  is defined as the thermal conductivity of the gas and the rate of viscous dissipation  $\psi$  is:

$$\psi = \frac{2\eta}{\rho} \left[ \left\| \frac{1}{2} \left( \frac{\partial v_\alpha}{\partial x_\beta} + \frac{\partial v_\beta}{\partial x_\alpha} \right) \right\|^2 - \frac{1}{3} (\nabla \cdot \vec{v})^2 \right] + \frac{\zeta}{\rho} (\nabla \cdot \vec{v})^2 \quad (2.13)$$

(e.g., Landau & Lifshitz, 1987, pg. 194). Comparison with equation (2.5) allows us to identify the contributions from the shear and bulk viscosities respectively. Instead of equation (2.7) a thermal energy equation like (2.12) is often evolved in hydrodynamic codes where the kinetic energy is likely to be comparatively

much larger. This ensures that the internal energy will not become negative due to small integration errors (Price, 2004).

Assuming an ideal gas, the equation of state  $P = (\gamma - 1) \rho u$  (where  $\gamma$  is the adiabatic index, and is constant for a polytropic<sup>1</sup> gas: 7/5 for a diatomic gas, and 5/3 for a monatomic gas) along with appropriate boundary conditions fully specifies this system (equations (2.1), (2.6), and (2.12)), collectively called (in the viscous case) the Navier-Stokes equations.

### 2.1.2 The SPH Method

Smoothed particle hydrodynamics (SPH) was developed by Lucy (1977) and then Gingold & Monaghan (1977). Reviews by Monaghan (1992, 2005) and Price (2004) explore this method in detail. A continuous fluid is decomposed into discrete particles that move with the flow. In this so-called *Lagrangian* formulation, the derivatives are co-moving, necessitating the use of the material derivative (2.2) in the gas dynamics equations. As such, explicit advection terms are not required, so bulk gas flows, including orbital motion, are correctly modelled. The major practical advantage of this formulation is that it is naturally adaptive; regions with greater densities will necessarily have a greater number of particles sampling that region of fluid, while low density regions will be sparsely populated. In contrast to grid schemes, complex geometries pose no additional problems. A smoothed form of any fluid quantity

---

<sup>1</sup> A polytropic gas has the property of pressure varying inversely with volume to some power (Landau & Lifshitz, 1987).

$A$  can be calculated for each particle  $i$ , using a volume-weighted contribution of values from neighbouring particles  $j$ , and is known as the “interpolant”  $\tilde{A}_i$ :

$$\tilde{A}_i = \sum_j^n A_j \frac{m_j}{\rho_j} W(\vec{r}_i - \vec{r}_j, h_i, h_j) \quad (2.14)$$

where  $A_j$  is the unsmoothed fluid quantity  $A$  at particle  $j$ ,  $m_j$  is the mass of fluid particle  $j$ ,  $\rho_j$  is the density at particle  $j$ , and  $h$  is a characteristic length scale called the smoothing length. Using integration by parts, derivatives can be transferred from  $A$  to the weighting function  $W$ .

The weighting function or *kernel* must be normalized, and must become a delta-function in the limit of  $h \rightarrow 0$ . The kernel typically resembles a Gaussian, but is usually constructed from a cubic-spline function to truncate the summation over a finite number of neighbours  $n$ . In three dimensions, the following form for the kernel is given by Monaghan (1992):

$$W(\vec{r}_{ij}, h_i) = \frac{1}{\pi h^3} \begin{cases} 1 - \frac{3}{2}r_h^2 + \frac{3}{4}r_h^3 & \text{if } 0 \leq r_h \leq 1 \\ \frac{1}{4}(2 - r_h)^3 & \text{if } 1 \leq r_h \leq 2 \\ 0 & \text{otherwise} \end{cases} \quad (2.15)$$

where we have defined  $\vec{r}_{ij} = \vec{r}_i - \vec{r}_j$  and  $r_h = r_{ij}/h_i$ . To satisfy Newton’s third law (momentum conservation), a symmetric kernel  $W_{ij} = W_{ji}$  is required to calculate forces between neighbours. This can be ensured by using a kernel-average  $W_{ij} = \frac{1}{2}(W(\vec{r}_{ij}, h_i) + W(\vec{r}_{ji}, h_j))$  (Hernquist & Katz, 1989). The characteristic width of the kernel is given by the smoothing length  $h$ , and is a measure of the spatial resolution of an SPH simulation.

Discretized versions of the Euler equations presented in §2.1.1 may be derived using the general form of the interpolant (2.14). Following Monaghan

(1992), the continuity equation is replaced by the SPH calculation for density of a particle:

$$\rho_i = \sum_j^n m_j W_{ij} \quad (2.16)$$

This formulation conserves mass exactly. The SPH form for the momentum balance equation (2.3) is usually written in symmetrized form:

$$\frac{d\vec{v}_i}{dt} = - \sum_j^n m_j \left( \frac{P_i}{\rho_i^2} + \frac{P_j}{\rho_j^2} + \Pi_{ij} \right) \nabla_i W_{ij} \quad (2.17)$$

which conserves both linear and angular momentum exactly (Monaghan, 1992). The gradient is taken with respect to the co-ordinates of particle  $i$ . The artificial viscosity term  $\Pi_{ij}$  will be discussed in §2.1.3.1. Finally, neglecting the physically dissipative and conductive terms, the specific internal energy equation (2.12) can also be written in symmetrized form, or alternatively (Evrard, 1988) as:

$$\frac{du_i}{dt} = \frac{P_i}{\rho_i^2} \sum_j^n m_j \vec{v}_{ij} \cdot \nabla_i W_{ij} \quad (2.18)$$

It can be shown (Wadsley et al., 2004) that equation (2.18) behaves similarly to formulations where internal energy is calculated via an entropy function (e.g., Lucy, 1977; Springel & Hernquist, 2002), which is dynamically evolved instead of the internal energy; as well, equation (2.18) is more robust than the symmetrized form in regions of highly variable pressure.

The simulations presented in this thesis use the parallel hydrodynamics code Gasoline (Wadsley et al., 2004). Gasoline builds on the  $N$ -body gravity code Pkdgrav (Stadel, 2001). The code uses a spatial binary tree to determine the hierarchical mass-distribution at each particle when calculating gravity, making the process  $\mathcal{O}(N \log N)$ , where  $N$  is the number of resolution elements

(in this case, particles) in the calculation. SPH summations are computed using a fixed number of neighbours  $\mathcal{O}(N)$ , which are found using a balanced  $k$ -dimensional, or K-D tree (Bentley, 1975). The K-D tree is a tree data structure composed of cells that correspond to regions in the simulation volume with approximately equal numbers of particles (Stadel, 2001). The implementation of the gas dynamics equations is mostly based on the one presented by Monaghan (1992), and summarized above. For computational efficiency, the current version of Gasoline computes a one-sided sum for density, that is, the kernel (2.15) is not averaged between neighbouring particles for the density calculation. Standard test results using this version of the code have not changed from those presented in Wadsley et al. (2004), which were performed using an averaged kernel. To retain momentum conservation, this change was not implemented for force calculations.

Time-integration is accomplished using a second-order leapfrog scheme, known as Kick-Drift-Kick (Quinn et al., 1997). For each iteration, particle velocities are first updated by a half-timestep (“half-kick”), followed by a full timestep position update (“drift”). Finally, the velocities are synchronized with the positions by another half-kick. A predictor step is used prior to the final half-kick to update the thermal energy and (SPH) acceleration (Wadsley et al., 2004). Gasoline assigns timestep sizes individually to particles, resulting in further efficiency.

### 2.1.3 Viscosity in SPH

#### 2.1.3.1 Artificial Viscosity

Numerical viscosity is required in all hydrodynamics codes to stabilize the scheme in question, and for SPH also to ensure proper entropy generation in shocks. Monaghan (1992) implements an explicit artificial viscosity by combining the term

$$\Pi_{ij} = \frac{-\alpha_{av}\bar{c}_{ij}\mu_{ij} + \beta\mu_{ij}^2}{\bar{\rho}_{ij}} \quad (2.19)$$

with the pressure terms within the parentheses in the momentum evolution equation (2.17), where  $c_i$  is the sound speed at particle  $i$  and

$$\mu_{ij} = \frac{h_{ij}\vec{v}_{ij} \cdot \vec{r}_{ij}}{|\vec{r}_{ij}|^2 + 0.01h_{ij}^2} \quad (2.20)$$

where  $\bar{c}_{ij}$ ,  $\bar{\rho}_{ij}$ , and  $h_{ij}$  are average quantities between neighbours, and  $\vec{v}_{ij} = \vec{v}_i - \vec{v}_j$ . The  $\alpha_{av}$  term in (2.19) (not to be confused with the *physical* viscosity parameter  $\alpha$  in equation (1.4)) produces artificial shear and bulk viscosities and the  $\beta$  term is needed to capture high Mach number shocks. The coefficients are typically assigned values of  $\alpha_{av} = 1$  and  $\beta = 2$  (Monaghan, 1992), but may be given other values to control the strength of the dissipation (as in §3.3).

The diffusion due to (2.19) should ideally be absent in non-convergent flows ( $\nabla \cdot \vec{v} > 0$  or, equivalently in SPH,  $\vec{v}_{ij} \cdot \vec{r}_{ij} > 0$ ) and minimized in rotating shear-flows such as disks. The use of constructs such as the Balsara (1995) switch is intended to accomplish the latter; the artificial viscosity term (2.19) is multiplied by the factor:

$$\frac{|\nabla \cdot \vec{v}|}{|\nabla \cdot \vec{v}| + |\nabla \times \vec{v}|} \quad (2.21)$$

averaged between neighbours. Equation (2.21) is  $\sim 1$  in regions of strong convergence ( $|\nabla \cdot \vec{v}|$  dominates) and is a minimum in regions of high vorticity ( $|\nabla \times \vec{v}|$  dominates), effectively reducing artificial viscosity in strongly rotating regions. The explicit dependence of (2.19) on the smoothing length means that numerical diffusion decreases with additional resolution and conversely increases with poorer resolution, which may be undesirable.

### 2.1.3.2 Physical Viscosity

As discussed in §1.2.1, viscosity controls angular momentum transport in accretion disks. Since this sets the accretion rate onto the disk's central object, it is essential that the transport of angular momentum is correctly reproduced in simulations. To better model the shear-stresses in rotating flows, we have added a true, physical viscosity into a version of Gasoline using the formulation described by Flebbe et al. (1994). Following this formulation, the gradient of the viscous stress tensor in SPH becomes:

$$\frac{1}{\rho} \sigma_{\alpha\beta,\beta} \Big|_{r=r_i} = \sum_j^n \frac{m_j}{\rho_i \rho_j} (\eta_i \sigma_{i\alpha\beta} + \eta_j \sigma_{j\alpha\beta}) W_{ij,\beta} \quad (2.22)$$

which may be added to the right hand side of equation (2.17) to give the SPH version of the viscous momentum conservation equation (2.6). The Gasoline implementation uses a two-sided summation for equation (2.22) but a one-sided summation for the viscous stress tensor (2.5) itself (see §2.1.2). The components of the tensor are given as:

$$\frac{\partial v_\alpha}{\partial v_\beta} = \sum_j^n \frac{m_j (\vec{v}_j - \vec{v}_i)_\alpha W_{ij,\alpha}(h_i)}{\rho_j} \quad (2.23)$$

omitting the bulk viscosity. Flebbe et al. also give an energy equation that may be compared with the differential version (2.12). This expression was not included in the Gasoline implementation since all simulations for this thesis were performed with a fixed temperature profile.

### 2.1.4 Sinking Particles

The tests performed in this thesis compare three different models of accretion centres for simulations of star-formation:

1. A non-accreting, collisionless particle (“star”) or a fixed  $r^{-1}$  gravitational potential imposed at the origin. Gravitational calculations are subject to a softening parameter  $\epsilon$  which is intended to prevent divergence in the gravitational forces at the origin<sup>2</sup> by smoothly decreasing the force to zero there, thus setting a gravitational-resolution limit (and effectively, a minimum timestep) for gas-particles (see e.g., Wadsley et al., 2004). Since we are not concerned with gravitational accuracy *interior* to the dense accretor in this work,  $\epsilon$  is set approximately equal to smallest initial particle separation. Similarly, a minimum smoothing length (chosen to be some fraction of  $\epsilon$ ) is sometimes imposed to set a minimum SPH-resolution (e.g, Petitsclerc, 2009), however, this removes the requirement of a fixed number of neighbours, and the SPH method locally becomes  $\mathcal{O}(N^2)$  rather than its usual  $\mathcal{O}(N)$ . A minimum smoothing length is not used in this work.

---

<sup>2</sup> Or more generally, between two self-gravitating particles as their separation vector  $\rightarrow 0$ .

2. Sink particles following Bate et al. (1995) without the explicit boundary corrections at the accretion radius advocated for therein (see §1.3.1). Particles within the accretion radius are immediately accreted onto a point mass based on energetic and dynamical considerations. This is the method for sinks currently available in Gasoline, and will be referred to in this work as “standard” sinks.
3. A sink particle formulation based on Bate et al. (1995); however, particles interior to the accretion radius are evolved kinematically, thus acting as a boundary condition at the accretion radius. A gas particle that crosses the accretion radius  $r_{\text{acc}}$  (subject to the normal Bate et al. criteria) is tagged as “sinking” (figure 2.1). An inwards spiralling Keplerian trajectory for the particle is calculated from its radial and tangential velocities  $(v_{r_0}, v_{t_0})$  when it crossed the threshold using:

$$v_r = v_{r_0} \tag{2.24}$$

$$v_t = v_{t_0} \left( \frac{R}{R_{\text{acc}}} \right)^{-1/2} \tag{2.25}$$

Since the future motion of the sinking particles is thus analytically determined, they are not included in the calculation for timesteps. As they in-spiral, the sinking particles can however act as neighbours for normal gas particles exterior to the accretion radius. This is intended to prevent the problems associated with having an evacuated region inside the sink (e.g. an artificial pressure gradient or unphysical angular momentum transport, leading to enhanced accretion). Further, the finite lifetime of a sinking particle limits how long angular momentum can be transferred from a particle inside the sink to the rest of the simulation.

Hydrodynamic quantities are not retained for these particles; to conserve momentum, any forces applied to sinking particles are added directly to the sink. Sinking particles are finally removed from the simulation as in the Bate et al. sinks, when they reach a user-defined radius, usually  $\leq 0.1r_{\text{acc}}$ . The sinking particle's mass is added to the sink at this point.

## 2.2 Constructing Initial Conditions

Care must be taken in constructing a particle distribution that is in a “relaxed” or minimum-energy state at the start of a simulation. Since particle locations are in a relaxed state at the end of a run, using this type of distribution for an initial condition ensures that the fluid is optimally sampled at the outset as well. For particles of equal mass, this also helps avoid any transient behaviour that may occur upon starting a simulation with a more regular initial distribution. This relaxed state is also known as a “glass”, because of the absence of crystalline structure, in analogy with real glass. Non-uniformities in the distribution are gradually smoothed out by evolving the distribution dynamically to an equilibrium configuration, subject to a damping force. All simulations performed in this thesis used equal mass particles; the use of variable mass particles or a different form for the kernel (2.15) will result in a different relaxed state (Monaghan, 2005).

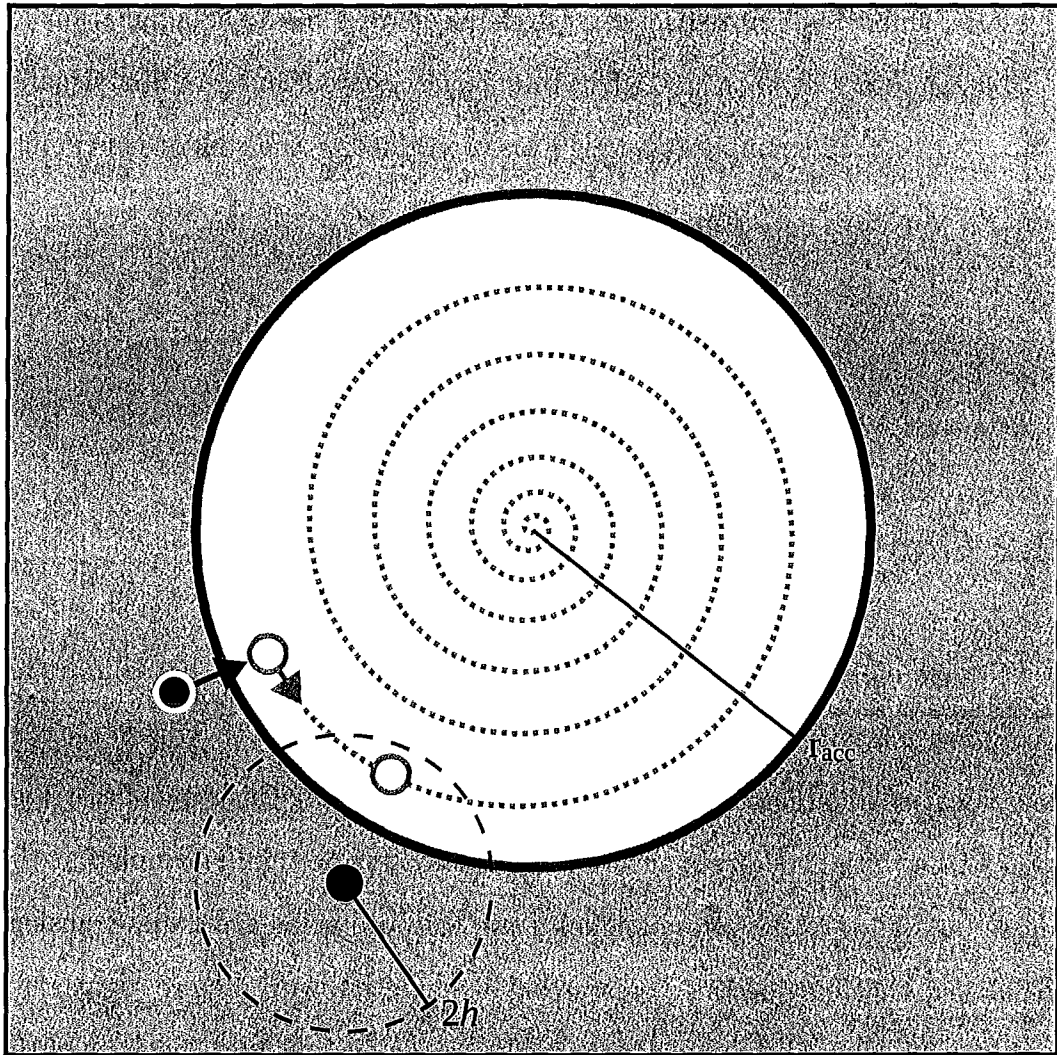


Figure 2.1: “Sinking particles” inner boundary condition. A gas particle that satisfies the criteria for accretion (solid, outlined) is now tagged as sinking (hollow). The sinking particle follows a spiral trajectory given by its velocity as it crosses the accretion radius. Sinking particles that fall within the interaction region of a normal gas particle (solid) act as neighbours for that particle.

### 2.2.1 Singular Isothermal Sphere

The singular isothermal sphere (SIS: Shu, 1977) was presented as a test of spherical accretion by Krumholz et al. (2004) and Cha & Whitworth (2003), and will also be presented here. The desired initial state is a  $1 M_{\odot}$  sphere containing  $\sim 50000$  gas particles arranged in a  $r^{-2}$  radial density profile. A standard periodic glass box containing  $16^3$  gas particles arranged in a uniform density was replicated until the desired number of particles were present, resulting in a unit-box centred on the origin. Next, the Cartesian coordinates for the particles were re-scaled by multiplying each coordinate by the radial distance vector squared (i.e. by  $r^2 = x^2 + y^2 + z^2$ ), with particles beyond  $r = 1$  removed, thus yielding an  $r^{-2}$  density profile for the unit-sphere. The sphere of particles was then allowed to relax in a fixed gravitational potential corresponding to a radial acceleration of  $a_r \propto r^{-1}$ , subject to an equation of state where  $T \propto r^2$ ; particle velocities are damped as they move toward a uniform pressure state corresponding to the desired density distribution. When particle motions became negligible the evolution was halted; particle velocities were zeroed in all directions, and assigned a temperature of  $T = 29$  K. The temperature chosen must be small enough that the sphere remains unstable at the centre and must match the external pressure at the edge of the sphere (see §3.1), but is otherwise arbitrary.

### 2.2.2 Keplerian Ring

To verify the implementation of physical viscosity in Gasoline, the evolution of a pressureless ring of viscous gas in a Keplerian orbit ( $v_{\phi} \sim r^{-1/2}$ ) at  $R = R_0$

and total mass  $m$  about a  $1 M_{\odot}$  star was simulated. The initial state for this test presented in Pringle (1981) specifies the surface density as  $\Sigma = \Sigma_0 \delta(R - R_0)$  where  $\Sigma_0 = m/2\pi R_0$ , and  $\delta(R - R_0)$  is the Dirac delta function. The subsequent evolution is given according to an analytic expression:

$$\Sigma(x, \tau) = \frac{m}{\pi R_0^2} \frac{1}{\tau x^{1/4}} \exp\left(\frac{-1 + x^2}{\tau}\right) I_{1/4}\left(\frac{2x}{\tau}\right) \quad (2.26)$$

where  $x = R/R_0$ ,  $\tau = 12\nu t/R_0^2$ ,  $\nu = \eta/\rho$  is the kinematic viscosity, and  $I_{1/4}$  is the modified Bessel function of the first kind of order  $1/4$ . For the initial condition, we used the surface density profile of the solution (2.26) at dimensionless time  $\tau = 0.016$ . The standard glass box was replicated  $16 \times 16$  times in the  $xy$  plane, and a slice  $1/16$  thick was taken in the  $z$ -direction to create a  $256^2$  glass in two dimensions. A particle distribution matching the surface density at the given time was determined by a Runge-Kutta method, and was used to scale the radial positions of the particles in the 2D glass. To approximate the pressureless state, the isothermal gas was set to a temperature of  $T = 10^{-6}$  K. The ring was centred on the origin, and was truncated at inner and outer radii  $0.7 R_0$  and  $1.3 R_0$  respectively. Keplerian velocities were then applied to the particles.

### 2.2.3 Accretion Disk

Since a significant fraction of the mass accreted by a forming star is likely from a circumstellar disk, studying how this accretion would proceed in the presence of a sink is essential. Disk simulations previously presented in the literature may suffer from numerical issues (see §§1.3.1 and 1.3.2). Part of the reason for this may be due to choosing disk parameters that are numerically

intractable. To study the effect of introducing the sink, it is important to create a simple, yet fully three-dimensional disk model where the results from that model are not adversely influenced by numerics. Rather than choosing the most realistic disk parameters, we elected to model a disk where the physical structure, such as the scale height, was resolved at all radii.

The standard periodic glass box was again replicated to create a wafer-like structure composed of 322,776 particles, with an overall aspect ratio of  $H/R = 0.09$  (where  $R = \sqrt{x^2 + y^2}$  is the usual cylindrical radial coordinate), with the centre-of-mass at the origin. The surface density of the disk is constant out to  $R = 1$  and linearly goes to zero at  $R = 1.25$ . A surface density  $\Sigma \propto R^p$  where  $p > -2$  will guarantee a finite mass as  $R \rightarrow 0$ .

A temperature profile of  $T \sim (r + \varepsilon)^{-2}$  where  $\varepsilon = 0.05$  was imposed on the gas. This profile was motivated by the need for adequate vertical resolution throughout the disk. Assuming vertical hydrostatic equilibrium, the vertical acceleration from (2.3) is:

$$\frac{1}{\rho} \frac{\partial P}{\partial z} = \frac{\partial}{\partial z} \left[ \frac{GM}{(R^2 + z^2)^{1/2}} \right] \quad (2.27)$$

which in the thin-disk approximation ( $R_{disk} \gg z_{disk}$ ) becomes:

$$\frac{1}{\rho} \frac{\partial P}{\partial z} = -\frac{GMz}{R^3} \quad (2.28)$$

and using  $\partial P/\partial z \sim P/H$  and  $z \sim H$ , along with the specified temperature profile, the resulting scale-height  $H$  for a disk in orbit around a central mass  $M$  should vary as

$$H \simeq c_s \left( \frac{GM}{R^3} \right)^{-1/2} \sim R^{1/2} \quad (2.29)$$

(Frank et al., 1985), which is a smoothly varying function throughout the disk.

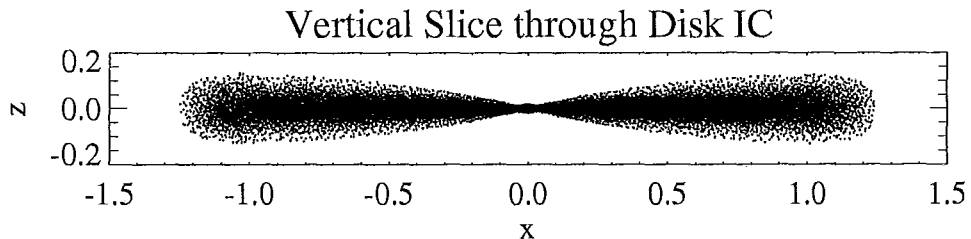


Figure 2.2: The initial state for accretion disk simulations: a slice  $y > |0.05|$  through the disk is shown.

To recover this vertical profile, the disk was relaxed vertically in the fixed potential of a  $1 M_{\odot}$  homogeneous spheroid of radius  $0.05 R_{disk}$  at the origin, with self-gravity switched off and an external pressure approximately equal to the minimum thermal gas pressure at the edge of the disk. All (cylindrically) radial accelerations and velocities in the disk plane were zeroed at every timestep, and the radial positions  $R$  were fixed. Particles were free to move in the vertical direction subject to a damping force, until vertical motions approached a minimum.

At this stage, the disk particles were assigned circular velocities to balance the radial component of gravitational acceleration in the disk plane due to the spheroid potential. The resulting initial condition for future simulations is shown in figure 2.2.

As a final note, Shen (2006) found that the scale-height in simulated disks should be resolved by several particle spacings to prevent artificial fragmentation. Since the disk inside  $r = 0.05$  will be unresolved by construction (due to

the presence of a sink of accretion radius  $r_{\text{acc}} \geq 0.05$ ), we found a minimum ratio of scale-height to smoothing length  $h \approx (m/\rho)^{1/3}$  at this radius of:

$$\frac{H}{\Delta x} \approx \frac{H}{h} \approx 9 \quad (2.30)$$

where  $m$  and  $\rho$  are the gas-particle mass and density, which indeed satisfies this criteria.

## Chapter 3

### Results

#### 3.1 Isothermal Collapse

A singular isothermal sphere (Shu, 1977) was created following the method in §2.2.1, and as previously tested with sinks by Krumholz et al. (2004) and Cha & Whitworth (2003). An isothermal sphere is initially in a  $r^{-2}$  radial density profile, with a fixed confining pressure. While the sphere is initially in hydrostatic equilibrium, the nature of the density distribution makes the central region unstable to collapse. A standard sink particle was placed at the centre of the sphere, immediately initiating a collapse under self-gravity.

The sphere was composed of 50,025 gas particles of total mass  $1 M_{\odot}$ ,  $r_s = 4125$  AU in radius. The gas was set to a temperature of  $T = 29.4$  K and an external pressure of  $P_{ext} = 7.6 \times 10^{-10}$  dyne  $\text{cm}^{-2} \approx \rho(r_s) c_s^2$  was applied. The central sink particle was  $2 \times 10^{-5} M_{\odot}$  with accretion radius  $r_{acc} = 124$  AU, and was incorporated without any inner boundary corrections.

As described in Shu (1977), the expected behaviour is an inside-out collapse, as layers of static gas above already in-falling material experience a

pressure gradient, thus acquiring an inward radial velocity. As a result, an expansion wave propagates outward from the accretion centre at the sound speed  $c_s = 3.3 \times 10^4 \text{ cm s}^{-1}$ . This is manifested as a “knee” in the radial density profile (figure 3.1) where the gas interior to the wave follows  $\rho \propto r^{-3/2}$ . The collapse time  $t_{collapse} = (GM_s)/(0.975 c_s^3)$  is defined as the time necessary for the sink to accrete all of the matter in the surrounding singular isothermal sphere (Cha & Whitworth, 2003). In particular, note that  $t = 0.5 t_{collapse}$  corresponds to the time when the rarefaction head hits the edge of the sphere. At this point, the entire sphere is in free-fall with  $v \propto r^{-1/2}$ . The accretion rate onto the sink remains constant at  $dm/dt = 0.975 c_s^3/G$  (McKee & Ostriker, 2007) until all of the mass has been accreted (figure 3.2).

The scatter (“noise”) in the density and velocity distributions gives an estimate of the uncertainty in the simulation result. In this respect, the mean values of the particle distributions of both quantities compared favourably with the exact solution given in Shu (1977) (i.e. are within the noise) around the location of the expansion wave head, which itself propagated at the correct rate. The greatest deviation from the exact result was in and around the sink itself. Although qualitatively correct, the average density of the in-falling gas was deficient inside the sink at early times, and enhanced at later times as one approaches the sink. This is in phenomenological agreement with a Godunov-type SPH simulation by Cha & Whitworth (2003). Similarly, the magnitude of the radial velocity of the gas inside the sink appeared to be (on average) overestimated early on and underestimated approaching the sink later. This did not, however, seem to cause large errors in the accretion rate.

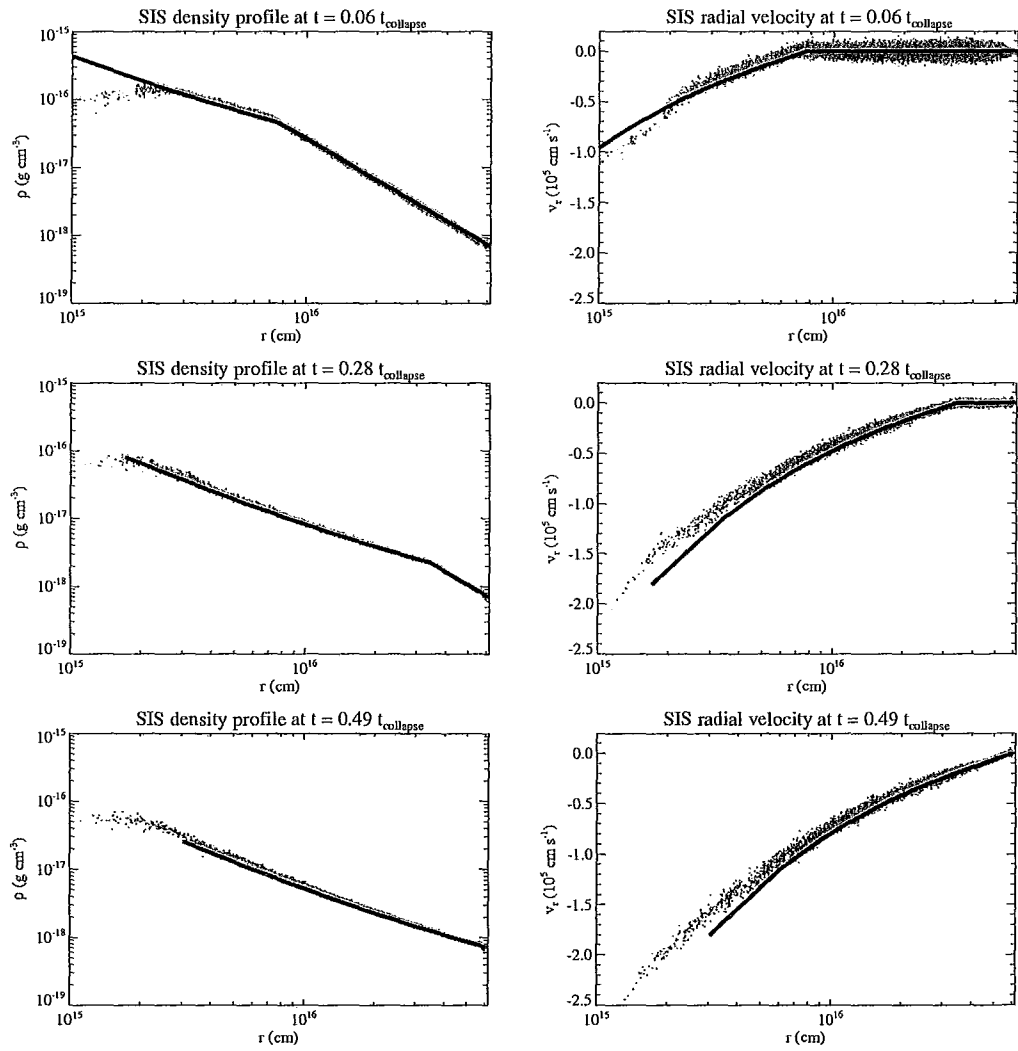


Figure 3.1: The density and radial velocity profiles of the SIS at different fractions of  $t_{\text{collapse}} = 3.73 \times 10^{12}$  s. The exact solution from Shu (1977) is plotted as a solid line over the result from the simulation.

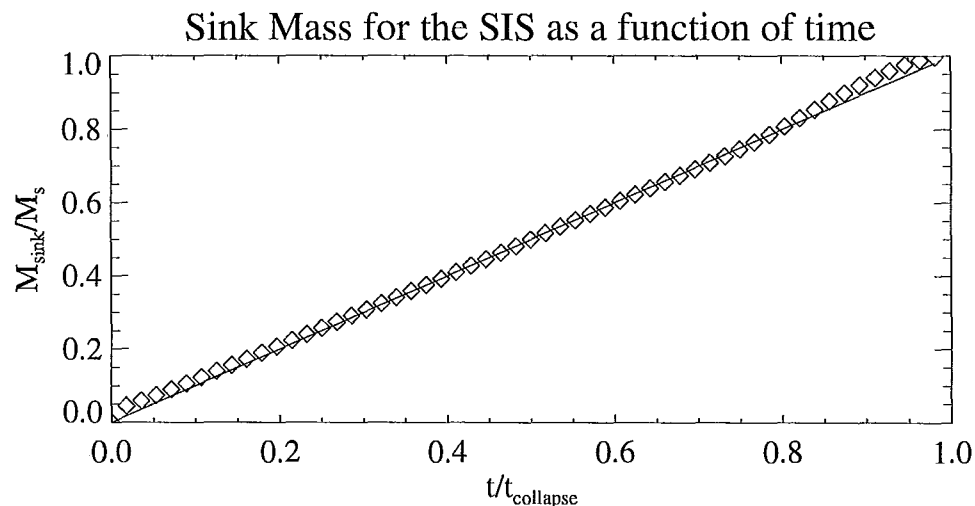


Figure 3.2: The accretion of mass by the central sink particle ( $M_{sink}$  in units of total sphere mass  $M_s$ ) as a function of total collapse time. The diamonds indicate the numerical result and the solid line is the analytic expectation.

In particular, the accretion rate was constant, and matched the theoretical expectation well. Upon starting the simulation, the accretion rapidly reached the correct rate at the correct sink mass; from  $t = 0.35$  to  $0.8$  the deviation from the expected mass was less than 0.1%. The slight discrepancy at late times can be attributed to worsening spatial resolution, as most of the initial sphere was accreted. We conclude that spherical accretion, for a static particle accreting from a static gas, was well modelled by this sink. Similar agreement was found using the sink implementation in Krumholz et al. (2004), in addition to the Cha & Whitworth (2003) results, who used the Bate et al. sink method.

## 3.2 Viscous Keplerian Ring

To better model the shear viscous force in our disk simulations, we have added physical viscosity into a version of Gasoline using the formulation described by Flebbe et al. (1994) (see §2.1.3.2 for a detailed description). To test the implementation, the evolution of a ring of gas particles in a Keplerian orbit was simulated. The ring was set up to be approximately pressureless so that it evolves only under gravitational and viscous forces. Viscosity acts to spread out the surface density profile; a ring annulus will impart angular momentum to an annulus that is radially exterior. Consequently, the exterior annulus gains orbital energy, whereas the interior annulus loses both orbital energy and angular momentum, moving radially inward. This process happens at all radii throughout the ring. The result is that most of the mass eventually spirals into the central accretor while most of the angular momentum is transferred to parts that subsequently move radially outward (Frank et al., 1985). This diffusive process is completely driven by viscosity (see §1.2.1).

The ring was composed of 12,784 particles of total mass  $m = 3 \times 10^{-6} M_{\odot}$  that were placed in a Keplerian orbit centred on  $R_0 = 1 R_{\odot}$  around a standard sink particle of mass  $1 M_{\odot}$ , and accretion radius  $r_{\text{acc}} = 0.0038 R_{\odot}$ . The gas particles were set to a temperature of  $T = 10^{-6}$  K. The ring was allowed to evolve viscously, with the constant kinematic viscosity set to  $\nu = 7.7 \times 10^{14} \text{ cm}^2 \text{ s}^{-1}$ . The evolution of the surface density of such a ring is given by Pringle (1981) via the scale-free equation (2.26).

The surface density evolution of the ring shown in figure 3.3 matches the analytic expectation and proceeds at the appropriate viscous timescale. Some

spurious waves were seen to propagate in the surface density profile but do not appear to alter the global behaviour of the ring. Only 45 particles, or approximately 0.35% of the initial gas was accreted by the sink by  $\tau = 0.171$ .

The evolution of the identical ring was also simulated without physical viscosity (i.e.  $\nu = 0$ ). Any spreading of the ring in this case would be due entirely to numerical effects, such as the artificial viscosity (2.19) or more complex forms of numerical diffusion (e.g., Krumholz et al., 2004). The artificial viscosity coefficient was set to the commonly used value of  $\alpha_{av} = 1$ .

The inviscid ring was observed to retain its surface density profile to several dynamical times (figure 3.4). Calculating the RMS of the binned-profile about  $R_0$  suggests that some minor diffusion occurred by 40 orbital times; at  $t = 40T$  the RMS was  $\langle (R - R_0)^2 \rangle^{1/2} = 1.09$  compared to the initial RMS of 0.179. Despite this, this still demonstrates the efficacy of the Balsara switch in suppressing artificial viscosity within shear flows at this resolution. By  $t = 40T$ , 95 particles, or about 0.7% of the initial ring was accreted by the sink. By comparison, 6.6% of the initial gas in the viscous ring was accreted by  $\tau = 0.779$  (about 40 orbital periods at  $R = 1$ ). The relative behaviour of artificial and physical viscosity is examined further in the following section, particularly §§3.3.1 and 3.3.3.

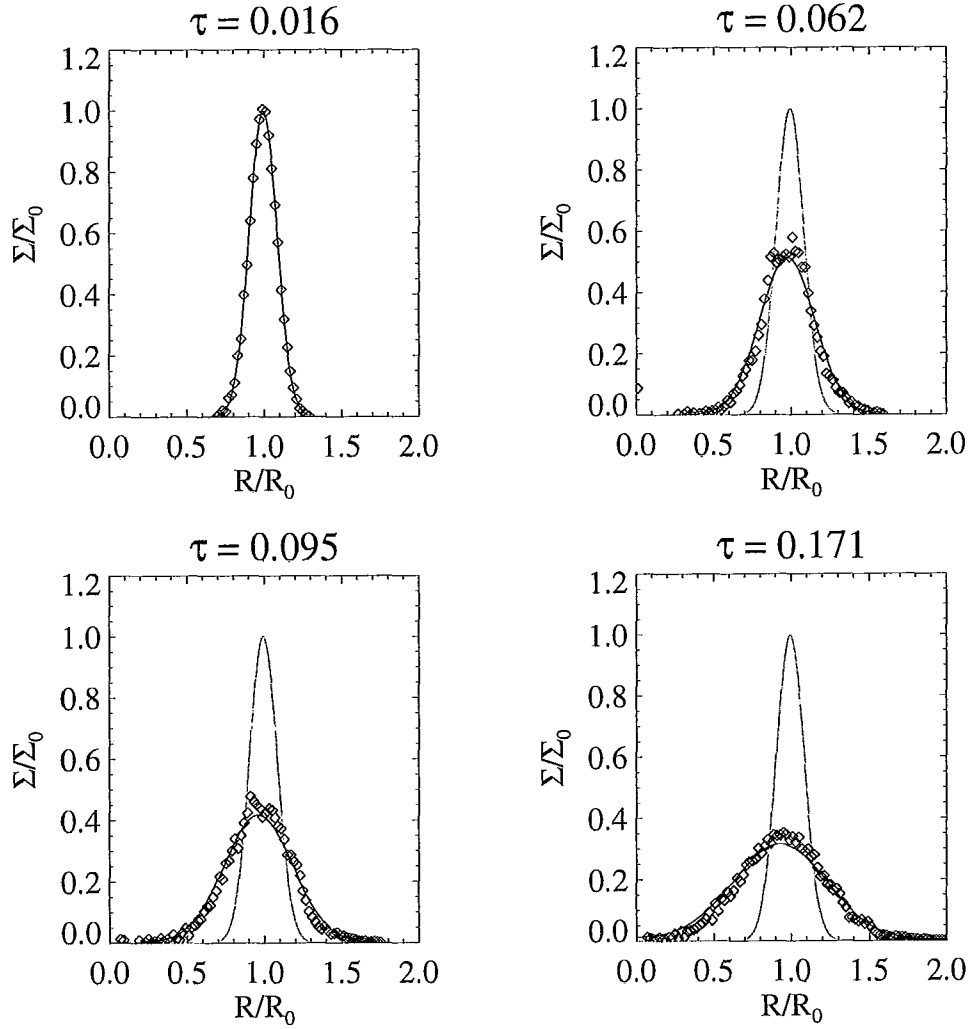


Figure 3.3: The surface density  $\Sigma$  of a viscous Keplerian ring in azimuthally averaged radial bins (diamonds) at various dimensionless times  $\tau$ .  $\tau = 0.171$  corresponds to about 8 orbital periods at  $R = R_0$ . The solid black line is the analytic solution for the same ring. The solid grey line shows the initial state.

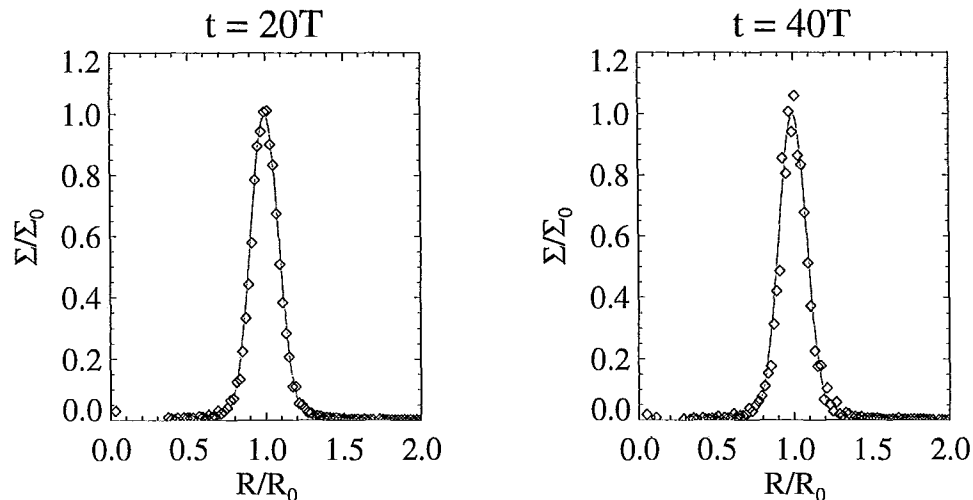


Figure 3.4: The surface density  $\Sigma$  of an inviscid Keplerian ring in azimuthally averaged radial bins (diamonds) at time in units of orbital period  $T$  at  $R = R_0$ . The initial surface density is shown by the solid grey line.  $40T$  is approximately  $\tau = 0.779$  for the same ring with  $\nu = 7.7 \times 10^{14} \text{ cm}^2 \text{ s}^{-1}$ .

### 3.3 Viscous Accretion Disks

#### 3.3.1 Fiducial Case: $\alpha = 0.1$ , $r_{\text{acc}} = 0.05$

A disk initially at constant surface density and with a fixed temperature profile  $T = 5(r + \varepsilon)^{-2}$  (see §2.2.3) was evolved for 10 orbital periods at the initial “edge” of the disk (defined as the radius where the surface density is no longer constant (see §2.2.3), corresponding to  $R = 1$  code unit =  $2 \times 10^{15} \text{ cm} \approx 134 \text{ AU}$ ). The disk was in orbit around a standard sink particle of mass  $M = 1 M_\odot$  and accretion radius  $r_{\text{acc}} = 0.05$  code units. Physical viscosity was parametrized using  $\alpha = 0.1$  (see §1.2.2). A circumstellar envelope

was crudely modelled by applying a fixed external pressure of  $P_{ext} = 2.08 \times 10^{-9}$  dyne  $\text{cm}^{-2}$ , intended to help confine the disk radially.

While this disk was at reasonably high resolution compared to disks in a typical star cluster simulation, the SPH *artificial* viscosity parameter was additionally lowered to  $\alpha_{av} = 0.1$  to ensure that evolution due to *physical* viscosity dominated. A rough estimate of the relative strengths of the artificial and physical viscosities can be made by approximating the artificial component as  $\nu_{av} = \alpha_{av} c_s h$  (where  $h$  is the SPH smoothing length); then for  $\nu > \nu_{av}$  the condition:

$$\frac{\alpha}{\alpha_{av}} > \frac{h}{H} \quad (3.1)$$

must be satisfied, where we have used the  $\alpha$ -prescription (equation (1.4)) for physical viscosity  $\nu$ . For this disk, this holds for all values of  $R$  (see equation (2.30)). This criteria does not take into account the effectiveness of the Balsara switch (equation (2.21)) in suppressing artificial viscosity; in the presence of the switch, physical viscosity may dominate even if the condition (3.1) is not strictly satisfied. For another comparison of artificial and physical viscosity in the disk simulations see figure 3.12.

All accretion disk tests were performed in the fixed homogeneous spheroidal potential (§2.2.3) with self-gravity turned off. This allowed us to study mechanisms for transport in disks apart from gravitational instability. This is well-justified in general if the Toomre parameter:

$$Q \equiv \frac{c_s \kappa}{\pi G \Sigma} \quad (3.2)$$

is larger than 1 for the disk under consideration (where  $\kappa$  is the epicyclic frequency,  $c_s$  is the sound speed, and  $\Sigma$  is the surface density). Physically,

this implies that the disk is stable to the growth of axisymmetric perturbations (Binney & Tremaine, 1987, pg. 362). For the Keplerian disk used in the simulations presented here, the epicyclic frequency  $\kappa$  is equal to angular rotation rate  $\Omega$ , giving a minimum  $Q \sim 50$  at  $R = 1$ , implying that the disk is very stable to both the formation and growth of spiral modes and gravitational fragmentation. Comparison between runs performed with self-gravity on and off gave identical outcomes, confirming that transport due to gravitational torques in this disk is negligible. In addition, the run with self-gravity calculations omitted finished approximately twice as quickly.

If other timescales of interest are much longer than the viscous timescale  $t_{visc} = R^2/\nu$ , the disk structure may be compared to the steady state case. Applying the  $\alpha$ -prescription for viscosity (§1.2.2) to this disk ( $c_s^2 \propto T \propto r^{-2}$ ) gives  $\nu \propto R^{1/2}$ . Assuming that a power-law surface-density profile  $\Sigma \propto R^p$  is an equilibrium solution for this disk in the steady-state, equation (1.9) gives  $v_r \propto R^{-3/2}$ . If time-derivatives vanish, equation (1.5) gives that the product  $R\Sigma v_R = -\dot{m}/2\pi$  is constant; to ensure this, the exponent in the surface density profile must be  $p = 1/2$  (if the power-law equilibrium solution is a valid assumption). The evolution of the surface density of the disk is plotted in figure 3.5, and a fit to the surface density at  $t = 1.4T$  is shown in figure 3.6.

It is important to recognize that the ideal steady-state model implicitly assumes a disk with a boundary at infinity, implying a divergent total mass as  $R$  extends to infinity. Such a situation is difficult to replicate in a simulation. Effects from the boundary do seem to alter the structure of the simulated disk

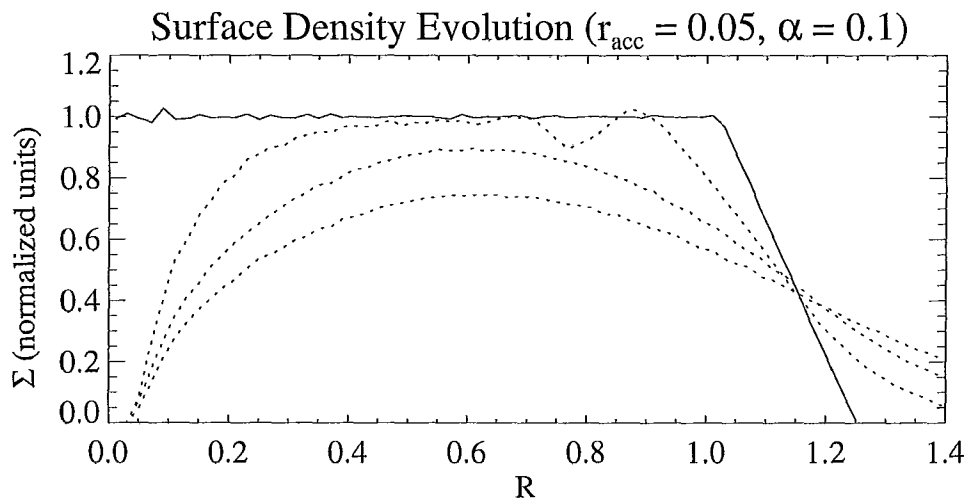


Figure 3.5: The azimuthally averaged surface density  $\Sigma$  of an  $\alpha = 0.1$  accretion disk at (dotted lines from top to bottom)  $t = T$ ,  $5T$ , and  $10T$  in units of the orbital period  $T$  at  $R = 1$ . The initial surface density is shown by the solid line.

fairly rapidly; in fact, no part of the disk can retain its initial surface density beyond  $t = 1.4T$ . The surface density profile at this time, however, does not readily appear to follow a simple power law over any radius in the disk. Two power-law fits are made to the inner region of the disk (where the evolution is not yet likely affected by the outer boundary) as shown in figure 3.6. Fits are made with exponents  $\sim 0.5$  and  $\sim 0.7$ . One can argue that both cases fit the profile equally well visually (e.g. within the uncertainties) in the inner-most region of the disk  $R \lesssim 0.3$ , but poorly elsewhere (e.g. out to  $R \sim 0.6$ ). As shown in figure 3.5, however, the surface density undergoes significant changes beyond the time  $t = 1.4$ , leading one to conclude that this disk is not likely to reach a steady-state at all; however the evolution does appear to follow the qualitative expectation for viscous disks. The global decrease in surface

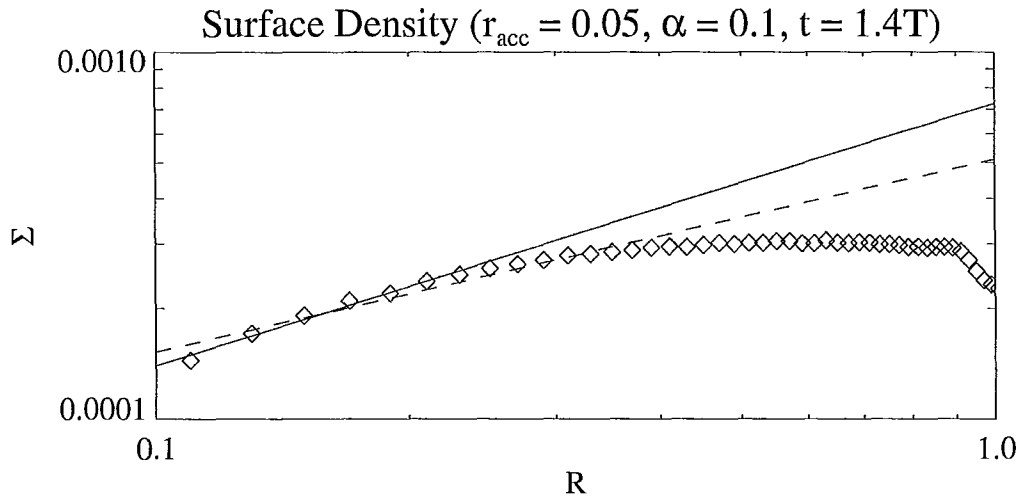


Figure 3.6: Least-squares fits to the surface density profile in code units at  $t = 1.4T$ . The dashed line is fit to a range  $R = 0.1 - 0.4$  with the result  $\Sigma \propto R^{0.53}$ . The solid line fit is performed over  $R = 0.1 - 0.25$  with the result  $\Sigma \propto R^{0.72}$ . If plotted, the binning uncertainties in the surface density profile at this scale would be slightly smaller than the size of the diamond symbols.

density implies that transport must be occurring, with the inner part of the disk initially in-falling and the outer part initially spreading.

While the surface density plots indicate that mass is moving inwards, figure 3.7 shows that the angular momentum distribution does in fact become weighted to larger radii as the simulation proceeds and the disk radius grows, again in agreement with viscous disk theory.

Transient features were also identified in this disk. A “kink” in the surface density was seen to propagate outward from the interior disk immediately upon starting the simulation. This was observed in all simulations using this disk, including ones without a central sink. This is likely due to an over-pressured

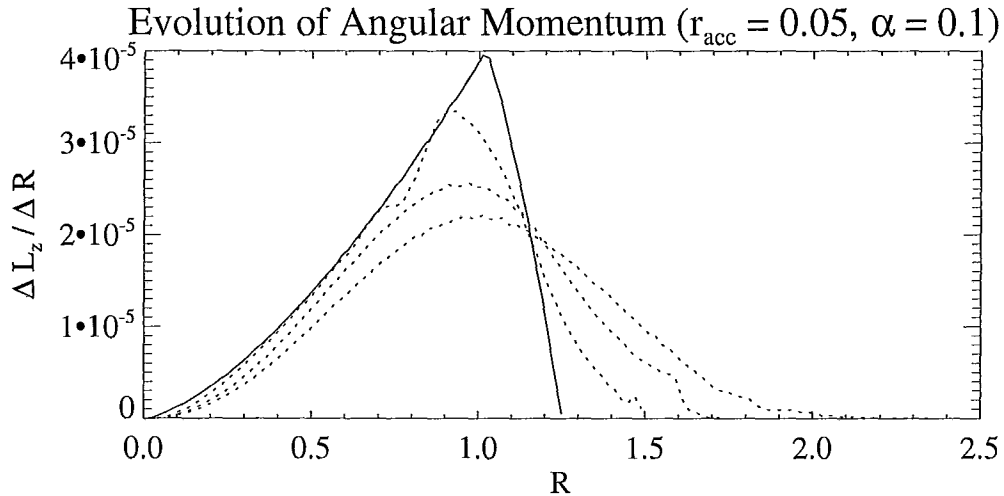


Figure 3.7: A comparison of the total  $z$ -component of the angular momentum (code units) in radial bins of width 0.02 in the fiducial disk at (dotted lines from top to bottom)  $t = T$ ,  $5T$ , and  $10T$  in units of orbital period  $T$  at  $R = 1$ . The initial angular momentum distribution is shown by the solid line.

interior region, making the velocities needed to balance gravity there slightly sub-Keplerian; the transient is probably a result of the disk adjusting to this. As well, the outer edge of the disk was initially seen to oscillate radially, however these oscillations slowly decay as the simulation proceeds, and the disk still showed an overall increase in radius, as expected for a viscous disk.

The accretion rate (1.10) can be related to the rate of change of the surface density via the continuity equation (1.5):

$$\frac{\partial \Sigma}{\partial t} = \frac{1}{2\pi R} \frac{\partial \dot{m}}{\partial R} \quad (3.3)$$

So for a steady disk, the accretion rate should also be constant throughout. The simulated disk, however, has a surface density that is everywhere *decreasing* with time, so plots of the accretion rate should show a negative slope. To

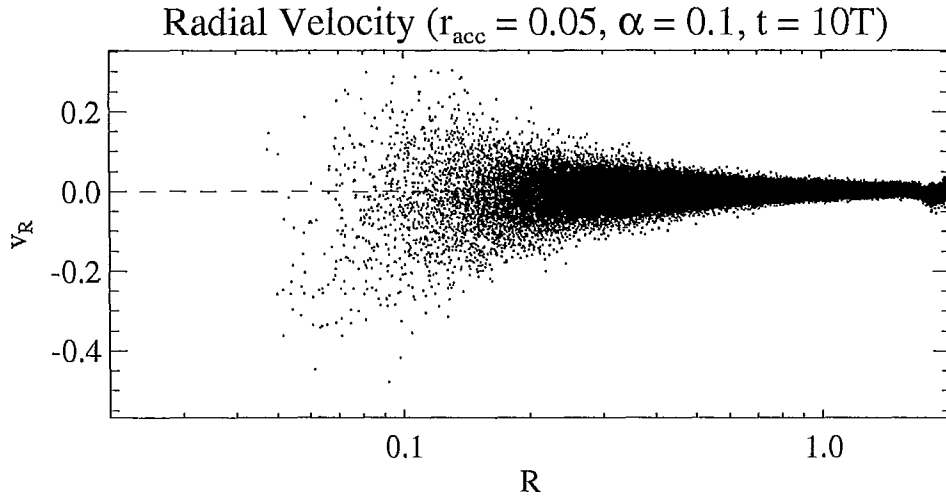


Figure 3.8: The particle distribution of radial velocities (code units) in the fiducial disk at  $t = 10T$ .

examine the accretion rate, an estimate of the radial velocity in the disk plane  $v_R = \sqrt{v_x^2 + v_y^2}$  is required. The expectation is that radial velocity will be negative near the accretion centre, and increasing with radius. Due to noise in the pressure forces within the simulated disk, the radial velocity distribution has a broad dispersion (figure 3.8).

The dispersion in velocities makes visually interpreting this representation of the data difficult. To get around this, the azimuthally averaged radial velocity in radial bins 0.02 code units in width was calculated (the disk is initially 1.25 code units in radius). The result is plotted in figure 3.9.

The averaged radial velocity profile is now clearly apparent. A root in this curve can now be identified where  $v_R < 0$  interior and  $v_R > 0$  exterior. This is a division between the parts of the disk where mass transport and angular

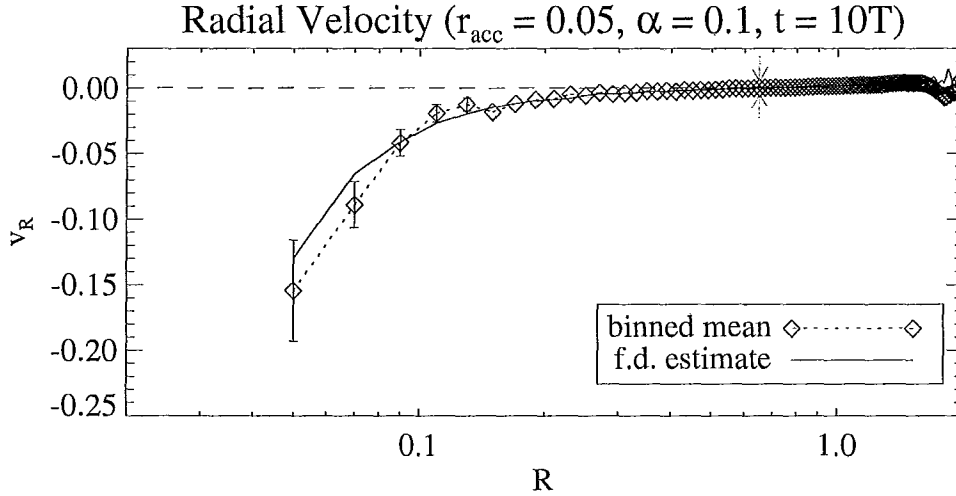


Figure 3.9: The mean radial velocity measured in radial bins of width 0.02 in the fiducial disk at  $t = 10T$ . Error bars (standard deviation of the mean) are plotted for points where the errors are larger than the diamond symbols at this scale. The grey arrows indicate the approximate location where  $v_R$  changes sign. A finite-difference (f.d.) calculation of  $v_R$  using equation (1.9) is over-plotted.

momentum transport successively dominate. This is also inconsistent with a steady-state disk, for as angular momentum moves outward, the transition radius (where  $v_R = 0$ ) moves outward as well, causing previously outgoing mass to fall inward. A finite-difference estimate of the radial velocity profile in a viscous disk using equation (1.9) and the measured surface density is also plotted, which the SPH estimate matches well qualitatively. The largest *percentage* deviations from the finite-difference curve are where the curve crosses the  $R$ -axis ( $v_R \rightarrow 0^-$ ), and near the outer edge, where the disk continues to undergo mild radial oscillations. Large percentage deviations are not unexpected in the former case since the value in the quotient will be nearly zero. Away

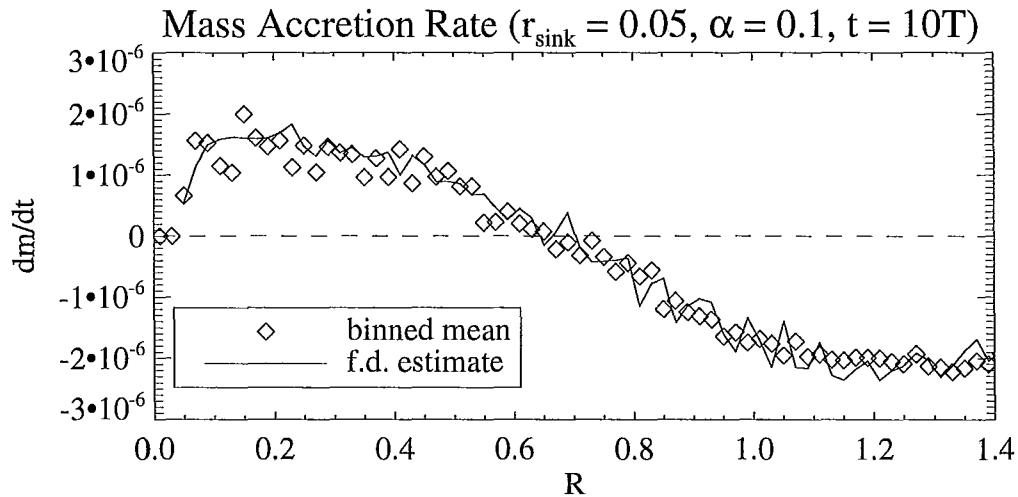


Figure 3.10: The accretion rate (1.10) (code units) in the fiducial disk as a function of position, calculated using the binned-average radial velocities (3.9). The expected curve using the finite-difference estimate for  $v_R$  is also plotted.

from these regions, the percentage deviation from the finite-difference curve is 10-20%. It is worth pointing out that the percentage deviation is within the same range in the inner-most region of the disk (near the sink), even though the absolute deviation may be larger.

A well-determined radial velocity profile allows the calculation of the radial mass flux, or accretion rate  $\dot{m}$  in the disk from equation (1.10) and the measured surface density. The resultant profile is plotted in figure 3.10, along with a finite-difference estimate using the finite-difference values of  $v_R$ .

As expected from equation (3.3), the curve has a negative slope across much of the disk, although it is nearly constant for a large portion of the inner disk. The region of greatest rate-of-change of  $\dot{m}$  appears consistent with figure 3.5 for the surface density evolution (and equation (3.3):  $\partial\Sigma/\partial t \propto \partial\dot{m}/\partial R$ ).

Interestingly, this seems to be at the radius in the disk where “decretion”, or outward mass flux begins. The exceptions to the negative slope are near the sink, where the surface density (and thus  $\dot{m}$ ) goes to zero, and the disk edge (not shown), where the oscillatory behaviour is altering the mass flux rate and surface-density rate-of-change. The binned-average and finite-difference curves match well, using the local spread of points in the binned-average accretion rates as an estimate of the uncertainties. The noisiness of the finite-difference curve is an artifact of its construction as a product of previous finite-difference calculations of the radial velocity and surface density.

The mass accretion history of the sink particle is plotted in figure 3.11. The sink immediately accretes the entire mass within  $r_{\text{acc}}$ . After this, the sink mass grows slightly sub-linearly with time, while the rate  $dm/dt$  decreases monotonically. It is unclear if the accretion rate at the sink will asymptotically approach a constant value. At 10 orbital times, the rate has dropped to  $dm/dt = 1.7 \times 10^{-6}$  code units. This value compares favourably with the accretion rate from in figure 3.10, using the approximately constant value in the region just beyond the sink of  $\dot{m} \sim 1.5 \times 10^{-6}$  code units.

Finally, a comparison of the contributions to the tangential acceleration in the disk can be made (figure 3.12). The SPH binned-averages for the total tangential acceleration match the finite-difference estimate well. The component due to just physical viscosity is nearly coincident with the total, and the artificial viscosity component is  $\sim 0$  throughout most of the disk. This serves as a check that the physical viscosity is dominant by 1-2 orders of magnitude, roughly agreeing with the estimate made in equation (3.1), although artifi-

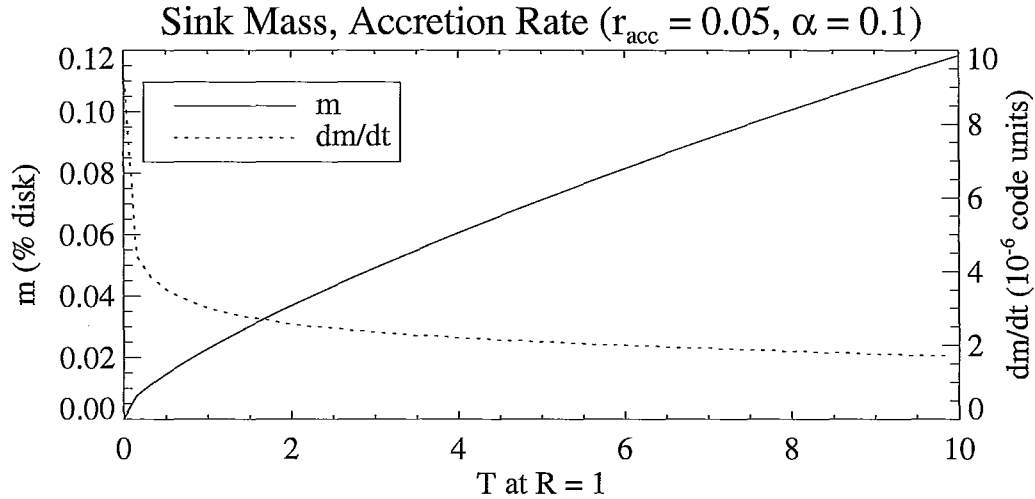


Figure 3.11: The sink mass and its accretion rate as a function of time in the fiducial case.

cial viscosity may be becoming a minor factor at  $R < 0.1$ . A change in sign at  $R \sim 0.7$  indicates a change in the direction of torques in the disk, which is yet another marker for the transition radius between radially-inward and radially-outward mass flux in the disk.

### 3.3.2 No-sink Case

The simplest method to avoid any potential pitfalls of using sink particles is to attempt a simulation without them. A goal for any sink formulation should be to reproduce the result from an identical case without sink particles. A simulation identical to the fiducial case from §3.3.1 is performed but without a central sink particle. An  $\alpha = 0.1$  viscous disk evolves in a  $1 M_{\odot}$  homogeneous

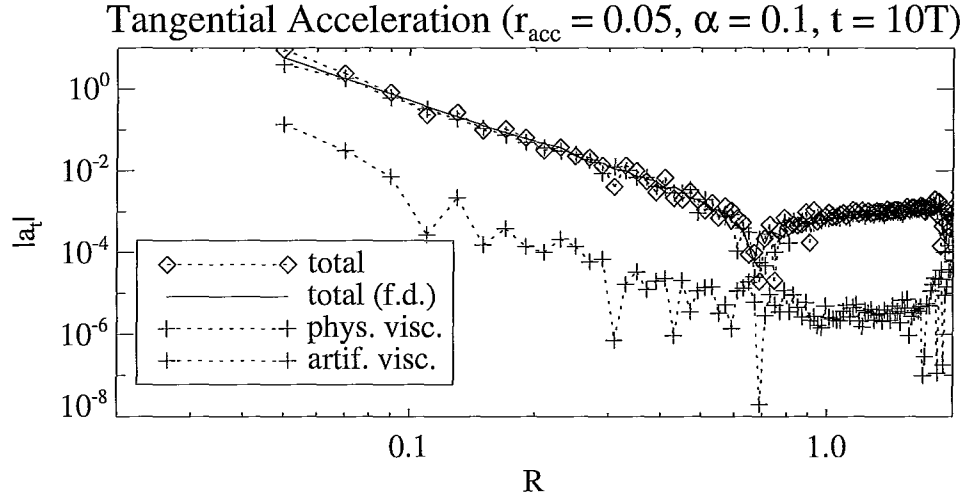


Figure 3.12: The artificial and physical viscosity components of the tangential acceleration in the fiducial disk at the end of the run. The total tangential acceleration and a finite difference estimate (f.d.) are also shown. Absolute values are plotted; the cusp at  $R \sim 0.7$  corresponds to a change in sign.

spheroid potential, and is subject to a gravitational softening length of  $\epsilon = 0.005$  code units in length, which is the same value as for the fiducial case.

While the shape of the mass-accretion curves are similar, the no-sink case has only accumulated about 7% of total disk mass within  $r < 0.05$  by  $t = 10T$ , whereas the sink accreted 12%; this is suggestive that the sink is causing artificial accretion in the fiducial case. The  $dm/dt$  curve exhibits the lower accretion rate for the no-sink case, and is also monotonically decreasing with time, albeit less smoothly than in the sink case.

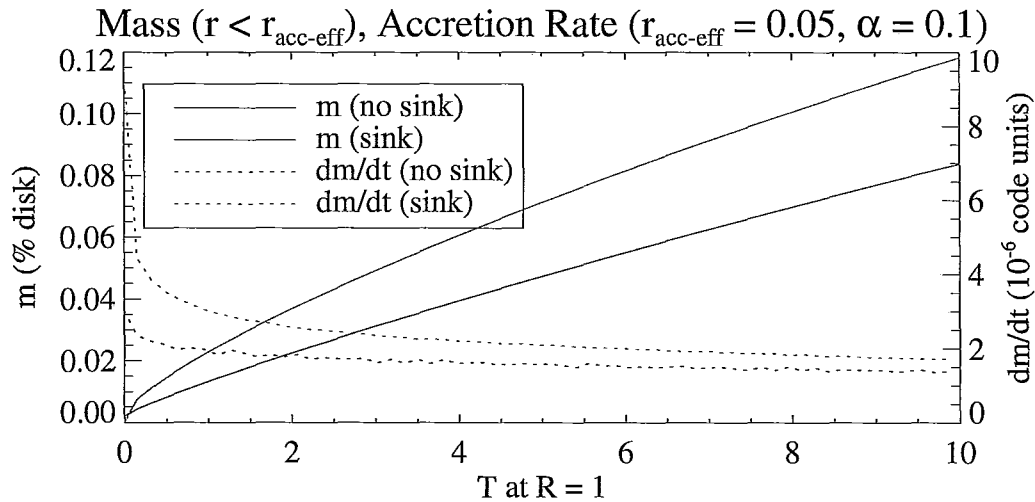


Figure 3.13: The mass contained within  $r < 0.05$  and the accretion rate for that region as a function of time in the no-sink case. The fiducial case is plotted in grey.

### 3.3.3 Varying $\alpha$

The  $\alpha$  parameter can vary widely between different accretion disks, and even within them (§1.2.2). Viscous evolution should occur on shorter timescales with larger values of  $\alpha$ . To test this, simulations identical to the fiducial case were performed with  $\alpha$  set to 0.2 and 0.4 respectively, and with standard sink particles.

Figure 3.14 demonstrates that the disks do appear to evolve faster with higher values of  $\alpha$ , with the  $\alpha = 0.4$  case showing the greatest radial in-fall velocities and accretion rates. For the same simulation time, the accretion radius in the mass accretion plots is greater with larger  $\alpha$ , further indicating that viscous evolution is proceeding faster. The SPH binned average estimates agree qualitatively with the finite-difference estimates with similar percentage

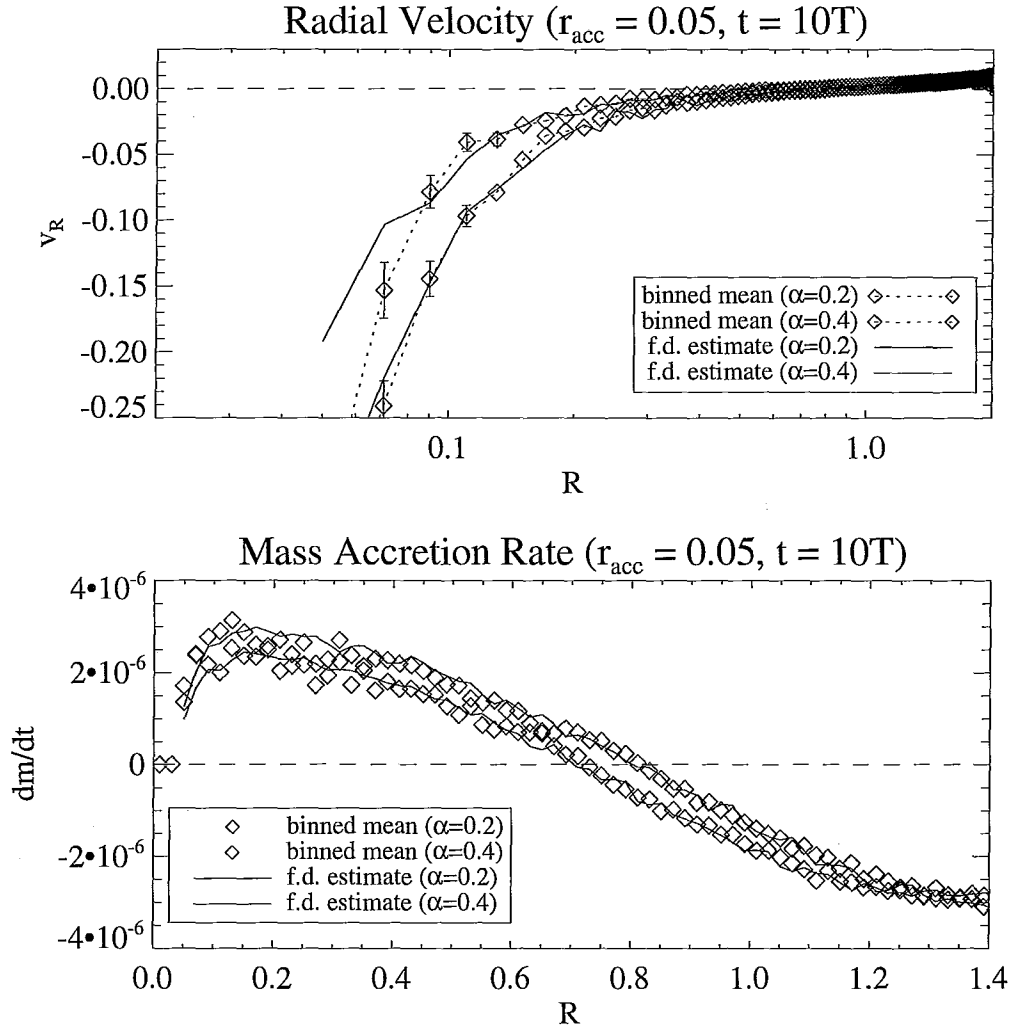


Figure 3.14: Binned-average radial velocities and mass accretion rates at  $t = 10T$  in the disks evolved with  $\alpha = 0.2$  and  $0.4$ . For clarity, a box-car smoothing of width 6 has been applied to the finite-difference (f.d) mass accretion rate estimates. The local spread in binned-average values estimate the uncertainty in the mass-accretion rates.

deviations to the fiducial case, demonstrating that the formulation is reasonably accurate over at least this range of  $\alpha$ .

Figure 3.15 shows that the sink mass growth is functionally similar even at larger  $\alpha$ , and an accretion rate of a few times  $10^{-6}$  is observed at late times independent of  $\alpha > 0$ . Although the accretion rate (1.10) scales linearly with radial velocity (and therefore viscosity), this is of course only true if the surface density is not changing greatly, which it surely is through most of the simulation. Very early in the simulation, one can argue for a rough linear relationship between the plotted accretion rate and  $\alpha$ . Note that a run with  $\alpha = 0$  is also plotted, and extrapolating this linear relationship suggests that the effective  $\alpha$  due to artificial viscosity alone is several times  $10^{-2}$ .

### 3.3.4 Varying the Accretion Radius

The accretion radius  $r_{\text{acc}}$  of the sink sets the spatial resolution of a simulation at that location. For relatively small changes in the size of the accretion radius, the dynamics of the simulation some distance away from the sink should not change. This was tested by simulating the fiducial case with a larger sink radius of  $r_{\text{acc}} = 0.1$ . The result is shown in figures 3.16 and 3.17.

A sink with a larger accretion radius can accrete a greater amount of mass in a disk, since the total mass flux is larger through a larger total (circumferential) surface area, although from equation (1.10), this also depends on how the radial velocity and surface density change with radius. To facilitate a comparison between the two cases, the mass of the sink in the fiducial case is replaced with the entire mass (sink + gas) within a radius of  $r = 0.1$ . When

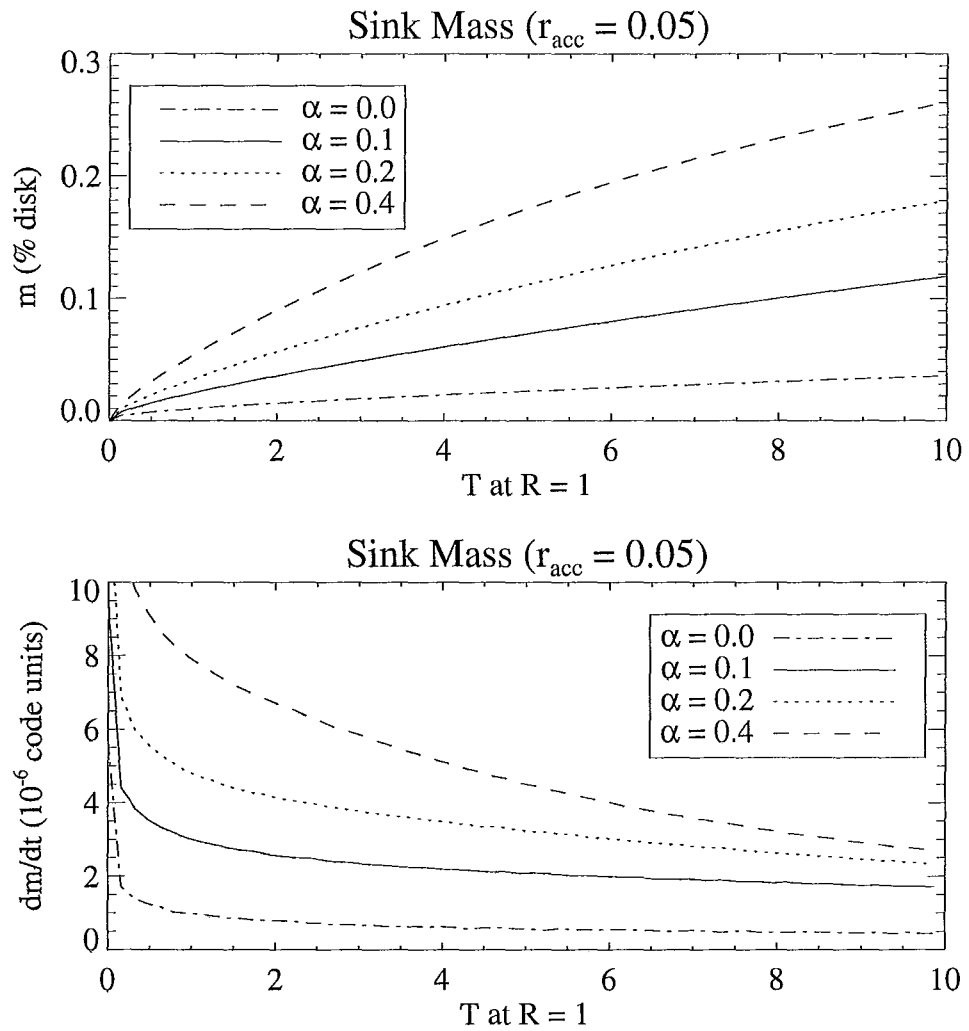


Figure 3.15: A comparison of the sink mass as a function of time for the disks evolved with  $\alpha = 0, 0.1, 0.2,$  and  $0.4$ .

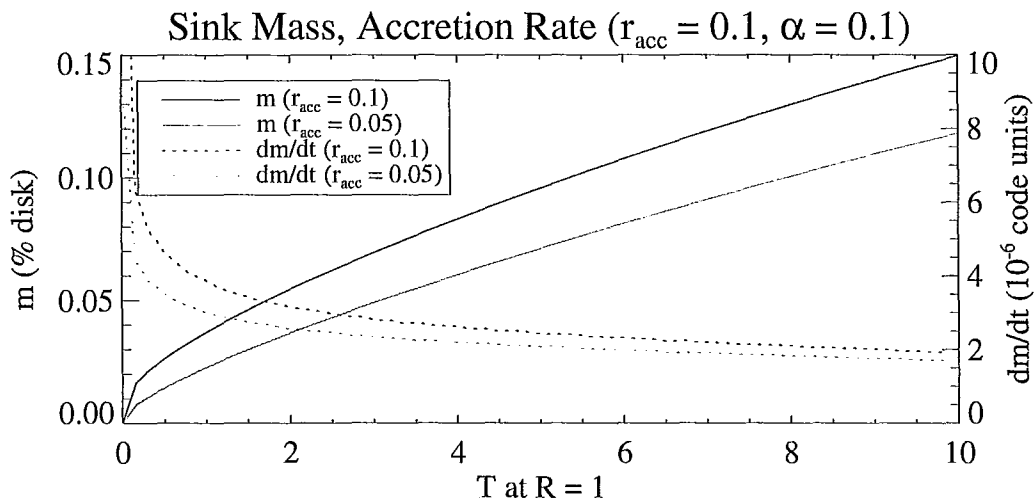


Figure 3.16: A comparison of the mass contained within  $r = 0.1$  and the accretion rate for that region as a function of time for the fiducial case ( $r_{\text{acc}} = 0.05$ ) and the  $r_{\text{acc}} = 0.1$  case.

the two runs with different accretion radii are compared this way, the accretion rates seem as if they are converging to a similar value at late times (figure 3.16), although they may remain offset from each other by a fixed amount. By this time, however, the larger accretion radius sink is about 20% heavier than the small accretion radius sink; even if the simulation is run longer and accretion rates become the same, this difference in sink mass will remain.

At the end of the simulation, figure 3.17 indicates that the accretion rate in the disk with the large accretion radius sink is marginally larger than the fiducial case from just beyond the sink accretion radii ( $R \sim 0.2$ ) to around  $R \sim 0.7$ , although the rates are nearly within uncertainties estimated from the local scatter in values. The negative mass flux in the outer, expanding part of the disks match fairly well between both cases, however the boundary may

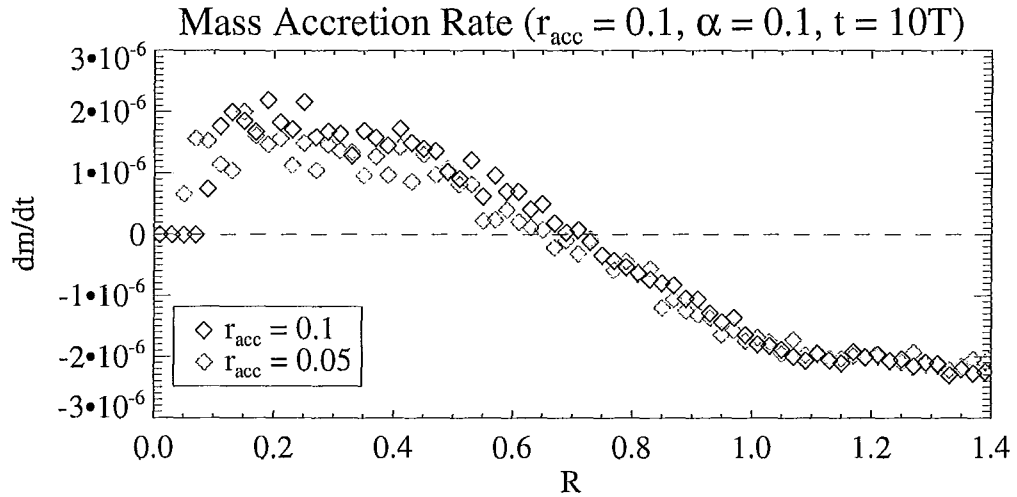


Figure 3.17: A comparison of the mass accretion rates (SPH binned averages) in the disk for the fiducial case ( $r_{\text{acc}} = 0.05$ ) and the  $r_{\text{acc}} = 0.1$  case.

be exerting an influence for  $R > 1$ . Evidently, one must choose an accretion radius with care if the final mass result is to be robust (see also Bate et al. (1995)).

### 3.3.5 Sinking Particles as a Boundary Condition

It may be that the artificial accretion observed in the fiducial case is in fact due to the lack of pressure support inside the sink and artificial angular momentum transport due to missing neighbours that was pointed out by Bate et al. (1995). A “sinking particles” boundary condition (described in §2.1.4) is applied to the sink in the fiducial case to investigate how this affects the accretion onto the sink.

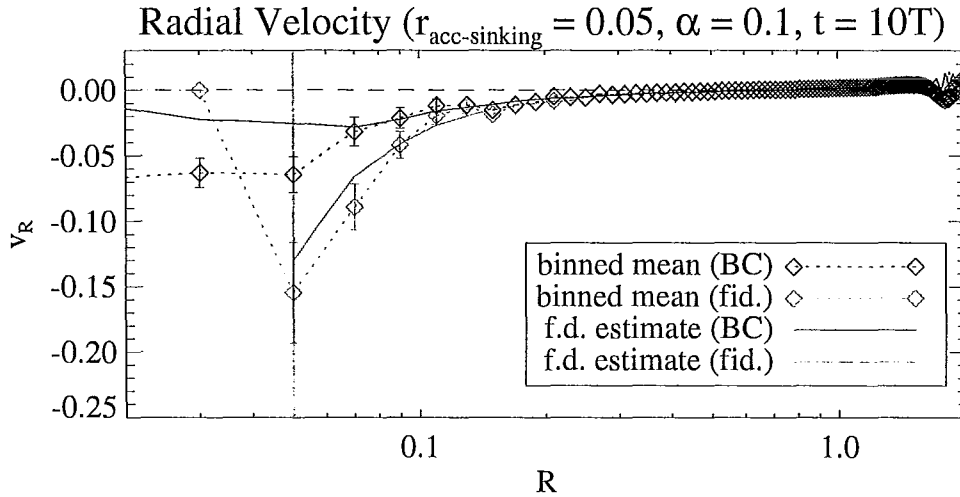


Figure 3.18: A comparison of the binned-average radial velocity in the fiducial case (fid.) and the case with a sinking-particles boundary condition (BC) as well as corresponding finite-difference estimate (f.d). The thick vertical line represents the sink accretion radii.

Figure 3.18 plots the radial velocity with a sinking particles boundary condition. Through most of the disk the binned-average and finite difference estimate agree qualitatively, particularly beyond the transition/decretion radius. The average  $v_R$  is constant interior to the accretion radius, as defined by the boundary condition. The finite difference estimate in this case suggests that the magnitude of the radial velocity is overestimated in this region. This overestimate is due to two factors: firstly, the surface density of the disk in this case does not go to zero inside the sink accretion radius, but instead spikes due to the extant sinking particles; secondly, the radial drift velocity of the sinking particles imposed at the accretion radius does not vary as the particles in-spiral within the sink. This can be contrasted with the fiducial case,

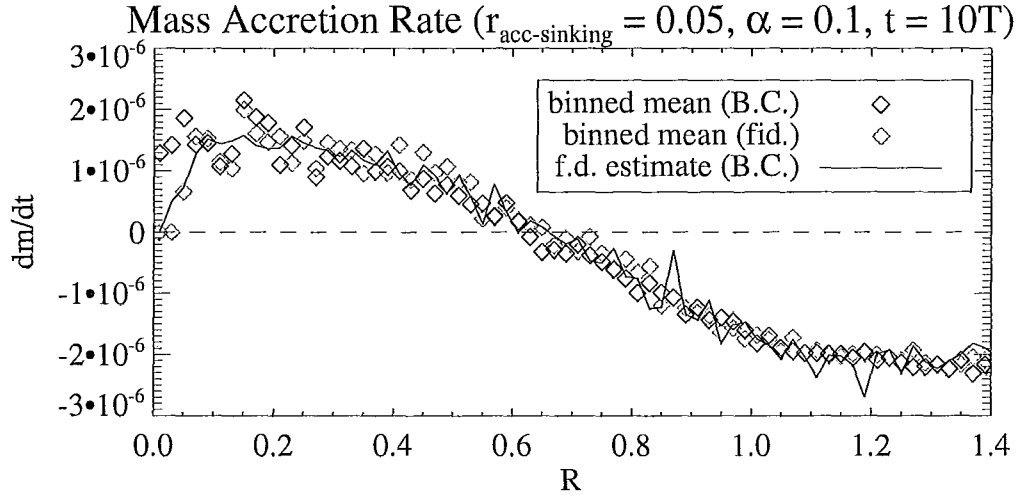


Figure 3.19: A comparison of the binned-average mass accretion rate in the fiducial disk (fid.) and the case with a sinking-particles boundary condition (B.C.). A finite-difference estimate for the accretion rate is also plotted for the case with the sinking-particles boundary condition.

where the radial velocity inside the sink immediately goes to zero (or rather, is undefined, as is manifest in the finite-difference estimate curve).

The mass-accretion in the disk (figure 3.19) can be explained by appealing to the same reasoning – interior to the sink, the binned-average accretion rate is roughly constant in the sinking particles case, and the finite-difference estimate is smoothly defined to  $R = 0$ . Figure 3.20 compares the mass in the sink with the standard sink case as well as the no-sink case.

It is clear that the sinking-particles boundary condition has inhibited accretion compared to the standard sink, however the total mass accreted is still larger than the no-sink case. While this is an improvement, the difference in final mass is still significant.

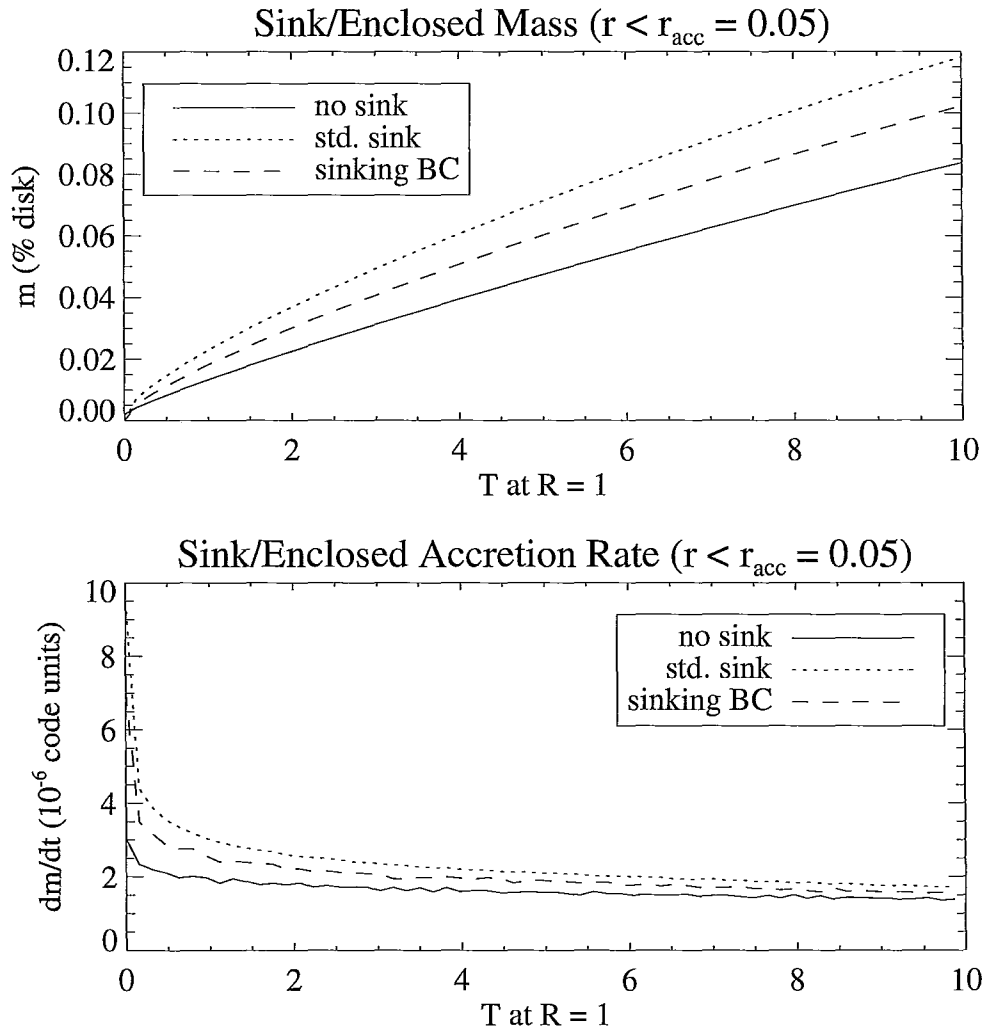


Figure 3.20: A comparison of the sink mass as a function of time in the fiducial, no-sink, and sinking-particles boundary condition case.

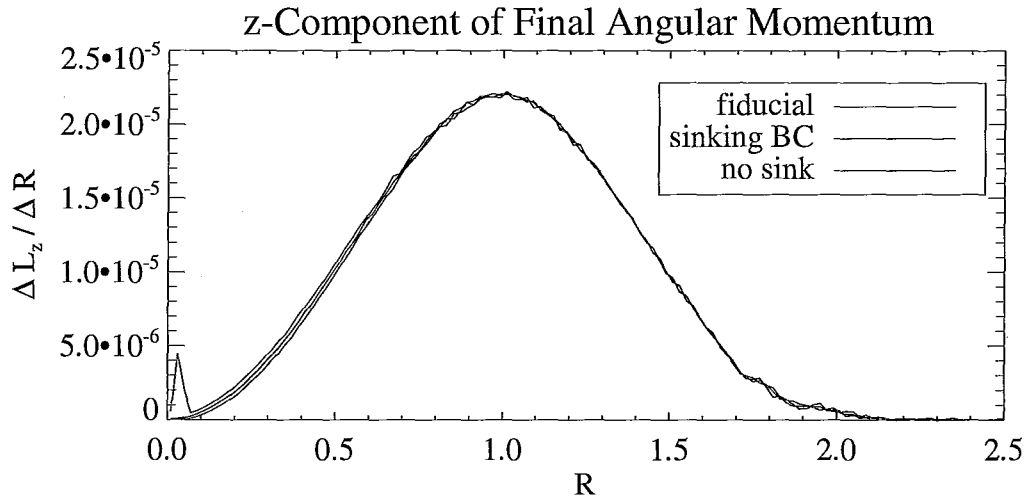


Figure 3.21: A comparison of the total  $z$ -component of the final angular momentum in radial bins of width 0.02 in the fiducial disk, the sinking-particles disk, and the standard sink disk.

### 3.3.6 Angular Momentum Distribution

As a comparison of the global behaviour of the disks with different central accretors, the total  $z$ -component of the angular momentum is plotted in radial bins (as in figure 3.7) at the conclusion of the simulations. The fiducial case, the no-sink case, and the sinking-particles boundary condition case are compared in figure 3.21.

The distributions in all three cases are nearly identical, and nearly coincident in the outer half. This indicates that angular momentum transport is behaving correctly on a global scale, especially in the region where outward transport is occurring. In the inner half of the distribution, the curves are vertically displaced (particular obvious from  $R \sim 0.5$  inwards), with the no-sink case largest, followed by the sinking-particles and standard sink cases. Inte-

Table 3.1: Comparison of Sink Mass at  $t = 10T$  in fractions of  $m_{disk}$ 

$r_{acc}$	BC	$\alpha$	$m(r < 0.05)$	$m(r < 0.1)$
n/a	n/a	0.1	0.0840	-
0.05	none	0.1	0.118	0.119
0.05	none	0.2	0.181	-
0.05	none	0.4	0.261	-
0.05	none	0.0	0.0369	-
0.1	none	0.1	-	0.150
0.05	sinking	0.1	0.103	-

grating these distributions shows that, indeed, the no-sink simulation has retained the most  $z$ -angular momentum, only losing 0.119% of the initial amount. The sinking case loses about 1.98%, and the standard sink case loses 3.10%. Some of the discrepancy can be accounted for by the spike in the distribution near the origin for the no-sink run, corresponding to a large number of gas particles that would otherwise have been accreted by a sink. A loss of some angular momentum from a disk to a protostar is expected, which in turn releases this via centrifugally driven outflows, but it is not clear how much should be lost.

Table 3.1 summarizes the amount of mass in the central accretor for all the cases presented. Standard sinks are labelled with “none” in the BC (boundary conditions) column. The no-sink simulation is labelled as “n/a” in both the BC and  $r_{acc}$  columns.

## Chapter 4

### Conclusion

The use of three different mechanisms for handling accretion processes in star-formation were investigated using the Gasoline  $N$ -body+SPH code: gravitational softening (or “no-sink”), “standard” Bate et al. sinks without boundary conditions, and a sink with a “sinking-particles” boundary condition.

Simulation of a singular isothermal sphere using a standard sink without boundary conditions gave results in good agreement with the exact solutions of Shu (1977). This suggests that boundary conditions are not required in cases with rapid isotropic accretion. The rapid rate of accretion may be why many groups, using different sinks (e.g., Krumholz et al., 2004; Cha & Whitworth, 2003), are able to successfully do this test.

We argue that tests of accretion onto sinks in rotating flows previously presented in the literature (Bate et al., 1995; Krumholz et al., 2004) are non-convergent due to the lack of a physically motivated process governing accretion in the simulation. Physical viscosity (e.g. via turbulence from the MRI – see §1.2.1) could potentially be used to serve this purpose. Physical viscosity was implemented using the Flebbe et al. (1994) formulation and tested on a

pressureless viscous ring in a Keplerian orbit; the time-evolution gave results matching the analytic expectation (Pringle, 1981). The identical test showed little evolution when performed without physical viscosity, suggesting that the artificial viscosity in Gasoline was diminished suitably in rotating shear flows using the Balsara switch, and  $\alpha_{av} = 1$ .

A high-resolution three-dimensional protostellar accretion disk with a well-resolved scale-height was evolved to investigate how accretion onto sinks behaves with physical viscosity. A number of results can be summarized:

1. The rapid evolution of the disk surface densities meant that they never reached a steady-state. It was concluded that steady-state disks are mainly useful as theoretical constructs, and not readily realizable in a simulation. Moreover, in a viscous simulation with a bounded disk radius, a steady-state is not possible due to angular momentum transport, which is clearly apparent in the simulated disks. Although steady-state disks also undergo this transport, their implied infinite extent means that angular momentum is transported to infinity, and there is an infinite reservoir of mass to replenish any changes in surface density.
2. Physical viscosity in the simulated disks was seen to dominate over artificial viscosity by up to a factor of 100 for the same value of the artificial and physical viscosity coefficients (i.e.  $\alpha_{av} = \alpha = 0.1$ ); this is in excess of a back-of-the-envelope estimate, implying that the Balsara switch again served its intended purpose. Values of  $\alpha$  that make up the lower range found in accretion disks (see §1.2.2) may then also be testable.

3. While the radial velocity distribution is noisy, the mean values in radial bins match qualitatively the expectation from a finite-difference estimate of the radial velocity using a closed-form expression. A similar agreement is found for the mass-accretion rate in the disk, particularly at radii that have a net outward mass-flux (e.g. figure 3.10). This holds for all cases presented.
4. The mass-accretion onto sinks was seen to follow a weak power-law over the time simulated, and increased with increasing  $\alpha$  (figure 3.15), or with a larger accretion radius (figure 3.16). From figure 3.15, the accretion rates onto the sinks for  $\alpha > 0$  varied within a factor of two after 10 orbital times, and the variably rapid initial accretion creates a hierarchy of final sink masses within a marginally larger factor.
5. A sink with “sinking-particles” interior to the accretion radius is tested as a possible inner boundary condition. The total mass-accreted is the closest to the non-sink simulation of all the variations presented, but is still not in complete agreement.

The velocity, mass-accretion rate, and angular momentum profiles all seem to indicate agreement with analytic estimates (or with each other, for the angular momentum) particularly well in the outer regions of the disk, defined as those regions with positive average radial velocities. In particular, the mass accretion rate in the disk beyond this radius did not show a dependence on the sink model (figures 3.19 and 3.17). One could potentially use this radius to identify the most trustworthy regions in sink simulations. There are, however, at least three problems with this: firstly, this radius is intended to move

outward with time, eventually beyond the majority of the mass in the disk, limiting its utility; secondly, this radius may be conservatively large – although the qualitative match to these quantities (radial velocity, mass accretion rate) may appear better in the outer regions, the percentage differences from the finite-difference calculations were in general not markedly improved over inner regions; thirdly, the outer regions of the disk may not have evolved long enough for discrepancies to appear.

## 4.1 Future Work

In addition to evaluating the modelling of physical viscosity itself, a main goal of this work is to evaluate if using a physical process to set accretion rates creates a situation where the use of sinks can be examined as a protostellar model. That the radial in-fall velocities of particles to be accreted matched the expected values is encouraging in this regard. An important point is what value should be used to assign a radial in-fall velocity to the sinking particles. In this implementation, the radial velocity used is that with which the candidate-particle crosses the accretion radius; however, as demonstrated in figure 3.8, the velocities can be rather noisy in this region. If a candidate-particle crosses the accretion radius with a very low radial-velocity, it takes an unrealistically long time to be accreted and remains tagged as “sinking” indefinitely. One option could be to use the the finite difference value, which agrees well with the binned-average. In simulations with self-gravity, gravitational instability can also drive transport processes within a disk; this can create an effective value of  $\alpha \sim 1$ , corresponding to a very high accretion rate. With these

concerns in mind, a finite-difference estimate for  $v_R$  may be best incorporated as a minimum radial velocity for sinking particles.

Both observations and theoretical considerations indicate that physical viscosity must be present in accretion disks, and that it is critical to disk evolution. Including physical viscosity in simulations is therefore well-justified. It is also well known that standard sinks over-accrete mass relative to equivalent no-sink simulations (§1.3.1). In the absence of a formal physical viscosity implementation, accretion disk simulations necessarily rely upon an artificial mechanism for accretion and angular momentum transport; such numerical mechanisms are unphysical. This will in general lead to incorrect results for star-formation (such as over-accretion). Our physical viscosity implementation in Gasoline gives the expected results for mass flux and radial velocity in an accretion disk, and should be included in any simulations claiming physical results involving accretion disks; however, over-accretion onto the central sink was still observed in the simulations presented. Since the mass accretion rate within the disk follows expectations from physical viscosity, and it was shown that artificial viscosity is negligible for the results presented in this work, further investigation into potential inner boundary conditions is likely warranted.

It should be noted that physical viscosity may be negligible in certain instances if some other transport process is dominating the evolution. Gravitational instability in a massive disk for instance can transport matter over large distances in a disk, with an effective  $\alpha$  much larger than that due to turbulent physical viscosity alone. If the accreted mass from the disk is not

replenished however (e.g. from a protostellar envelope), the importance of disk self-gravity will diminish, and a regime for physically viscous evolution may later be reached.

Running the disk simulations longer can also help determine if the variation in final sink-mass among the different models is retained. Since the disk becomes rarefied as it expands and since particles are continually removed from the simulation by the sink, a concern is ensuring that the disk remains at a high enough resolution everywhere at all times. Using lower values of physical viscosity can help to slow the accretion, however the timescale for viscous evolution varies inversely with viscosity, so very long integrations may be necessary to examine the behaviour throughout the entire disk. A “in-flow” outer boundary condition that can continually provide mass to the disk, effectively creating an infinite disk, could be helpful, although a straightforward method of implementing this does not currently exist.

The simulations examined here are all at high-resolutions. The target application for these sinks however is in star-cluster formation, where the resolution will be much poorer at the same physical scale. This means that the contribution of artificial viscosity will eventually be greater than physical viscosity, and will increase the rate at which particles are accreted. Additional work will need to be done on examining low-resolution counterparts of the disks presented here. While the Balsara switch has proven effective in high-resolution cases, a different treatment may be needed in low-resolution situations.

## Bibliography

- Alves, J., Lombardi, M., & Lada, C. J. 2007, *A&A*, 462, L17
- Andrews, S. M. & Williams, J. P. 2005, *ApJ*, 631, 1134
- . 2007, *ApJ*, 659, 705
- Balbus, S. A. 2003, *ARA&A*, 41, 555
- Balbus, S. A. & Hawley, J. F. 1991, *ApJ*, 376, 214
- Balsara, D. S. 1995, *JCoPh*, 121, 357
- Bate, M. R. 2009a, *MNRAS*, 392, 590
- . 2009b, *MNRAS*, 392, 1363
- Bate, M. R. & Bonnell, I. A. 2005, *MNRAS*, 356, 1201
- Bate, M. R., Bonnell, I. A., & Bromm, V. 2002, *MNRAS*, 332, L65
- . 2003, *MNRAS*, 339, 577
- Bate, M. R., Bonnell, I. A., & Price, N. M. 1995, *MNRAS*, 277, 362
- Bentley, J. L. 1975, *Communications of the ACM*, 18, 509
- Bergin, E. A. & Tafalla, M. 2007, *ARA&A*, 45, 339
- Binney, J. & Tremaine, S. 1987, *Galactic dynamics* (Princeton, NJ: Princeton University Press)

Bondi, H. 1952, MNRAS, 112, 195

Bondi, H. & Hoyle, F. 1944, MNRAS, 104, 273

Bonnell, I. A., Clark, P., & Bate, M. R. 2008, MNRAS, 389, 1556

Bonnell, I. A., Larson, R. B., & Zinnecker, H. 2007, in *Protostars and Planets V*, ed. B. Reipurth, D. Jewitt, & K. Keil, 149–164

Bromm, V., Coppi, P. S., & Larson, R. B. 2002, ApJ, 564, 23

Cha, S.-H. & Whitworth, A. P. 2003, MNRAS, 340, 73

Chapman, S. & Cowling, T. G. 1970, *The mathematical theory of non-uniform gases: an account of the kinetic theory of viscosity, thermal conduction and diffusion in gases* (Cambridge: Cambridge University Press)

Chorin, A. J. & Marsden, J. E. 1990, *Texts in Applied Mathematics, Vol. 7, A mathematical introduction to fluid mechanics*, 2nd edn. (New York: Springer-Verlag)

Clarke, C. J. & Carswell, R. F. 2007, *Principles of Astrophysical Fluid Dynamics* (Cambridge: Cambridge University Press)

de Pater, I. & Lissauer, J. J. 2001, *Planetary Sciences* (Cambridge: Cambridge University Press)

Evrard, A. E. 1988, MNRAS, 235, 911

Flebbe, O., Muenzel, S., Herold, H., Riffert, H., & Ruder, H. 1994, ApJ, 431, 754

- Frank, J., King, A. R., & Raine, D. J. 1985, *Accretion power in astrophysics*, Cambridge Astrophysics Series (Cambridge: Cambridge University Press)
- Gingold, R. A. & Monaghan, J. J. 1977, *MNRAS*, 181, 375
- Haisch, Jr., K. E., Lada, E. A., & Lada, C. J. 2001, *ApJL*, 553, L153
- Hartmann, L., Calvet, N., Gullbring, E., & D'Alessio, P. 1998, *ApJ*, 495, 385
- Hawley, J. F., Gammie, C. F., & Balbus, S. A. 1995, *ApJ*, 440, 742
- Hayashi, C. 1981, *PThPS*, 70, 35
- Hernquist, L. & Katz, N. 1989, *ApJS*, 70, 419
- Holland, W. S., Greaves, J. S., Zuckerman, B., Webb, R. A., McCarthy, C., Coulson, I. M., Walther, D. M., Dent, W. R. F., Gear, W. K., & Robson, I. 1998, *Nature*, 392, 788
- Hoyle, F. & Lyttleton, R. A. 1939, in *Proceedings of the Cambridge Philosophical Society*, Vol. 35, *Proceedings of the Cambridge Philosophical Society*, 405
- Isella, A., Carpenter, J. M., & Sargent, A. I. 2009, *ApJ*, 701, 260
- Kalas, P., Graham, J. R., & Clampin, M. 2005, *Nature*, 435, 1067
- Kalas, P., Liu, M. C., & Matthews, B. C. 2004, *Science*, 303, 1990
- Klessen, R. S., Krumholz, M. R., & Heitsch, F. 2009, arXiv:0906.4452 [astro-ph.IM]
- Krumholz, M. R., Klein, R. I., & McKee, C. F. 2007a, *ApJ*, 656, 959

Krumholz, M. R., Klein, R. I., McKee, C. F., & Bolstad, J. 2007b, *ApJ*, 667, 626

Krumholz, M. R., Klein, R. I., McKee, C. F., Offner, S. S. R., & Cunningham, A. J. 2009, *Science*, 323, 754

Krumholz, M. R., McKee, C. F., & Klein, R. I. 2004, *ApJ*, 611, 399

Lada, C. J., Muench, A. A., Rathborne, J., Alves, J. F., & Lombardi, M. 2008, *ApJ*, 672, 410

Landau, L. D. & Lifshitz, E. M. 1987, *Course of Theoretical Physics, Vol. 6, Fluid mechanics*, 2nd edn. (Oxford: Pergamon Press)

Larson, R. B. 1981, *MNRAS*, 194, 809

Lodato, G. & Rice, W. K. M. 2004, *MNRAS*, 351, 630

Low, C. & Lynden-Bell, D. 1976, *MNRAS*, 176, 367

Lucy, L. B. 1977, *AJ*, 82, 1013

Mac Low, M.-M. & Klessen, R. S. 2004, *Reviews of Modern Physics*, 76, 125

Masunaga, H. & Inutsuka, S.-I. 1999, *ApJ*, 510, 822

Matzner, C. D. & McKee, C. F. 2000, *ApJ*, 545, 364

McKee, C. F. & Ostriker, E. C. 2007, *ARA&A*, 45, 565

Monaghan, J. J. 1992, *ARA&A*, 30, 543

—. 2005, *RPPh*, 68, 1703

Mundy, L. G., Looney, L. W., & Welch, W. J. 2000, in *Protostars and Planets IV*, ed. V. Mannings, A. P. Boss, & S. S. Russell, 355–376

Padoan, P. & Nordlund, Å. 2002, *ApJ*, 576, 870

Petitclerc, N. 2009, PhD thesis, McMaster University

Price, D. J. 2004, PhD thesis, University of Cambridge

Pringle, J. E. 1981, *ARA&A*, 19, 137

Quinn, T., Katz, N., Stadel, J., & Lake, G. 1997, [arXiv:astro-ph/9710043](https://arxiv.org/abs/astro-ph/9710043)

Ruffert, M. 1994, *ApJ*, 427, 342

Shakura, N. I. & Sunyaev, R. A. 1973, *A&A*, 24, 337

Shen, S. 2006, Master's thesis, McMaster University

Shu, F. H. 1977, *ApJ*, 214, 488

Shu, F. H., Li, Z.-Y., & Allen, A. 2004, *ApJ*, 601, 930

Smith, B. A. & Terrile, R. J. 1984, *Science*, 226, 1421

Springel, V. & Hernquist, L. 2002, *MNRAS*, 333, 649

Stadel, J. G. 2001, PhD thesis, University of Washington

Vorobyov, E. I. & Basu, S. 2009, *MNRAS*, 393, 822

Wadsley, J. W., Stadel, J., & Quinn, T. 2004, *New Astronomy*, 9, 137

Ward-Thompson, D., André, P., Crutcher, R., Johnstone, D., Onishi, T., & Wilson, C. 2007, in *Protostars and Planets V*, ed. B. Reipurth, D. Jewitt, & K. Keil, 33–46

